Pure Appl. Chem., Vol. 79, No. 10, pp. 1691–1729, 2007.
doi:10.1351/pac200779101691

Defect-fluorite oxides $M_{1-y}Ln_yO_{2-y/2}$ (Ln = lanthanide; M = Hf, Zr, Ce, U, Th): Structure, property, and applications*

Akio Nakamura[1,‡], Nobuyuki Masaki[2], Haruyoshi Otobe[2], Yukio Hinatsu[3], Junhu Wang[4], and Masuo Takeda[4]

[1]Advanced Science Research Center, Japan Atomic Energy Agency, Tokai, Naka, Ibaraki 319-1195, Japan; [2]Nuclear Science and Engineering Directorate, Japan Atomic Energy Agency, Tokai, Naka, Ibaraki 319-1195, Japan; [3]Department of Chemistry, Hokkaido University, Sapporo 060-0810, Japan; [4]Department of Chemistry, Toho University, Funabashi, Chiba 274-8510, Japan

Abstract: An up-to-date summary of our coupled macroscopic (lattice parameter, a_0) and microscopic (Mössbauer) studies on the entitled systems is given, shedding new light on the basic phase and structure properties of these technologically important, highly defective oxides. Through these studies, the intermediate-pyrochlore (P)-based local structure nature of the so-called stabilized-zirconia (SZ)- and stabilized-hafnia (SH)-type defect-fluorite (DF) phases in the M^{4+} = Zr and Hf systems seems to be almost unambiguously established with different (from the conventional) approaches: These are (1) the presence of a broad lattice parameter (a_0) hump over the extended stabilized cubic DF region (y = ~0.3–~0.7); (2) the microscopic ^{151}Eu-Mössbauer evidence of Eu^{3+} isomer shifts (ISs) showing characteristic V-shaped minima around the ideal-P area (y ~ 0.50) for both the M^{4+} = Zr and Hf systems; and (3) rich ^{155}Gd-Mössbauer data on the $Zr_{1-y}Gd_yO_{2-y/2}$ system [IS, quadrupole splitting (QS), line width, peak height, and relative absorption area (RAA)], revealing detailed features of its ordered P–disordered DF phase and structure relationships. These results are discussed with reported basic-property data of these systems.

Keywords: defect-fluorite oxides; stabilized zirconia (hafnia); lattice parameter; non-Vegardian behavior; Mössbauer spectroscopy; powder X-ray diffraction; local structure; fluorite structure; pyrochlore structure; C-type structure.

INTRODUCTION

To gain insight into the basic phase and structure properties of the entitled so-called defect-fluorite (DF) oxides, $M_{1-y}Ln_yO_{2-y/2}$, i.e., grossly oxygen-deficit solid solutions formed between the F-type MO_2 (M^{4+} = Hf, Zr, Ce, U, Th) (Fig. 1a) and its superstructure derivative, the C-type sesquioxide, $LnO_{1.5}$ [Ln^{3+}(lanthanide) = La-Lu, Y, In, Sc, etc.] (Fig. 1b), we have been engaged in their coupled macroscopic (lattice parameter, a_0) and microscopic (Mössbauer) studies. Our prime interest here is in elucidating the controversial local structure nature of the so-called stabilized-zirconia (SZ)- and stabilized-hafnia (SH)-type "apparently powder X-ray diffraction (PXRD) metrically disordered" DF solid

*Paper based on a presentation at the 12th International IUPAC Conference on High Temperature Materials Chemistry (HTMC-XII), 18–22 September 2006, Vienna, Austria. Other presentations are published in this issue, pp. 1635–1778.

‡Corresponding author: E-mail: nakamura.akio@jaea.go.jp

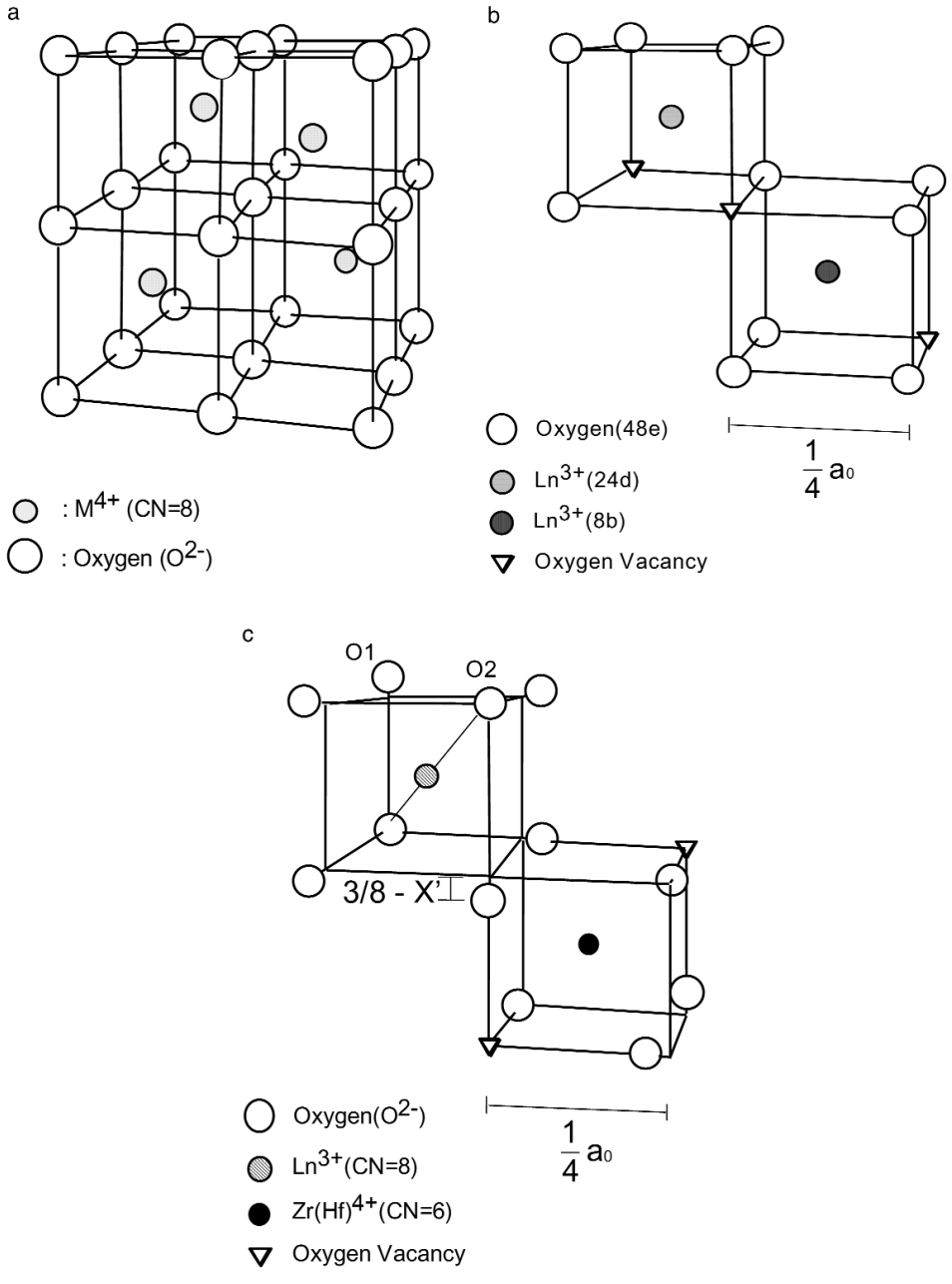

Fig. 1 (a) The parent F structure of the fluorite dioxide MO_2 at $y = 0$ [M^{4+} = (Zr), (Hf), Ce, Th, U, Pu, Am, etc.] (space group; Fm3m): The M^{4+} occupies the center of the oxygen cube (CN = 8). Oxygen (O^{2-}) occupies the center of the cation tetrahedron (CN = 4). (b) The C-type structure of the lanthanide (Ln) sesquioxide $LnO_{1.5}$ at $y = 1.0$ (superstructure of the fluorite structure shown in (a) with its lattice parameter doubled [a_0(C) = 2·a_0(F)] (space group; Ia3-Th[7]). The two kinds of Ln^{3+} sites (24d and 8b) exist. For each site, two oxygens around the Ln^{3+} (CN = 6) are either face- or body-diagonally missing, respectively. (c) The P structure of the intermediate $Ln_2Zr(Hf)_2O_7$ at $y = 0.50$ (superstructure of the F structure shown in (a) with its lattice parameter doubled [a_0(P) = 2·a_0(F)] (space group; Fd3m): The larger A^{3+} (= Ln^{3+}) is oxygen eight-coordinated (CN = 8) by two apical O2 and six more-distant O1 oxygens. The smaller B^{4+} [= $Zr^{4+}(Hf^{4+})$] is six-coordinated by O1 oxygens (CN = 6). Thus, two oxygen vacancies ($2V_O$) are adjacent to the smaller Zr^{4+}.

solution phases; whether these are indeed an intermediate pyrochlore (P)-type one as suggested by some recent extended X-ray absorption fine structure (EXAFS) and other results or not [1–3]. We intend to do this in a global scope including also the parent F-based M^{4+} = Ce, U, and Th systems with different approaches hitherto not used for this purpose.

As is apparent in many periodically appearing review articles [4–7], the basic phase and structure properties of these DF oxides have been the subject of numerous experimental as well as theoretical studies for a long time, for these have direct bearing on various key properties for their electrochemical and nuclear applications such as ionic conductivity, radiation tolerance, irradiation behavior, and long-term phase and thermal stability, etc. Among others, SZs have the widest applications also as superplastic ceramics, transition-toughened ultra-hard ceramics, thermal barrier coatings, catalysts, abrasives, and even synthetic jewels, etc. Their Hf analogs (SHs) are of interest as neutron-shielding/controlling devices, but are generally much less attended. Thus, these properties have been so far most thoroughly investigated for SZs, especially for yttria- and calcia-SZs (YSZ and CSZ, respectively). YSZ and CSZ are commercially available representative solid electrolytes (oxide-ion conductors) applicable for oxygen sensors/pumps, solid oxide fuel cells (SOFCs), etc. Experimental techniques hitherto employed in those studies include neutron-, X-ray- and electron-diffraction (ND, XRD, and ED) techniques and spectroscopic (EXAFS, XANES, Raman, NMR, ESR, γ-γ angular correlation, and optical, etc.) methods, thermodynamic (specific heat, enthalpy, oxygen potential, etc.) and dielectric/mechanical relaxation measurements, and so on.

The important difference of SZs (SHs) [M^{4+} = Zr(Hf)] from the parent F-based M^{4+} = Ce, U, and Th systems in this context is, besides their obvious (monoclinic to cubic-DF) "stabilized" nature realized by aliovalent-cation substitutions [$Zr^{4+}(Hf^{4+}) \rightarrow Ln^{3+}(Ca^{2+})$], for larger (early) Ln^{3+}(= La-Gd)-SZs (SHs), an intermediate P compound, $Ln_2Zr(Hf)_2O_7$, is formed at $y = 0.50$, accompanying some defect pyrochlore (DP)-type homogeneity range ($\sim 0.45 \leq y \leq \sim 0.55$) in the middle of such grossly oxygen-deficit "disordered" stabilized DF phases ($\sim 0.18 \sim 0.20 \leq y \leq \sim 0.60 \sim 0.80$) [1–5]: In the ideal (stoichiometric) P $A_2B_2O_7$ [8,9] (here A^{3+} = La-Gd, B^{4+} = Zr(Hf); Fig. 1c), both the cations (A^{3+},B^{4+}) and the oxygens are regularly ordered, so that the larger A^{3+} and the smaller B^{4+} are oxygen eight- and six-fold coordinated (CN = 8 and 6), respectively, thus, the two oxygen vacancies ($2V_O$s) are adjacent to the smaller B^{4+}. This first nearest-neighbor (1st NN) $Zr(Hf)^{4+}$-V_O association is just the reverse situation to the dopant [$Ln^{3+}(Ca^{2+})$]-defect(V_O) associate (complex) type description often supposed for these DF oxides [5,10,11].

One central concern of such basic-property studies of these DF oxides has been the characteristic ionic-conductivity maximum almost commonly observed for $LnO_{1.5}$(CaO)-SZs around the lower monoclinic/cubic-DF phase boundary region, i.e., around the minimum 12.5–16 mol % dopant[$Ln^{3+}(Ca^{2+})$] level (y = ~0.125–0.16) [5,10,11]: This corresponds to a low V_O concentration (in site fraction) of $[V_O] = y/4 = 0.03125$–0.04 for $LnO_{1.5}$-SZs (or $[V_O] = y/2 = 0.0625$–0.08 for CSZ = $Ca_yZ_{1-y}O_{2-y}$). Subsequent steady decrease of ionic conductivity with y inside the cubic-DF single-phase region indicates that more and more V_Os are becoming less mobile irrespective of its apparent increase in concentration. Since similar conductivity maximum is also observed for Ln^{3+} (Ca^{2+})-doped cerias and thorias [5,12,13], this has often been interpreted by the dopant($Ln^{3+}(Ca^{2+})$)-defect(V_O) complex model [5] and/or its extended version [10,11], among varieties of other qualitative proposals such as V_O ordering/clustering, V_O–V_O repulsion, local-distortion/strain effects, and a P (or other)-type microdomain formation, etc. In parallel, their numerous local structure studies have been carried out up to now, for ionic-conduction by V_O mechanism is likely to be more susceptible to the defect (V_O)-related local structure of the system rather than its long-range average structure.

In recent years, the increasing nuclear importance of SZs (nuclear waste form and inert matrix fuel (IMF), etc.) has been giving another incentive to such local structure study [14,15]. One major stimulus here is that the Gd-zirconate pyrochlore $Gd_2Zr_2O_7$ has recently been found to be much more radiation-tolerant than the corresponding titanate pyrochlore $Gd_2Ti_2O_7$ hitherto studied in the United

States as a prominent candidate for Pu immobilization [16–18]. Thoria (ThO_2), urania (UO_2), and their DF oxides are known to be quite radiation-tolerant from their long history as oxide nuclear fuels. Especially, UO_2, its burnable poison $U(Gd)O_2$, and the mixed-oxide (MOX) $U(Pu)O_2$ are the representative commercial nuclear fuels almost exclusively used in the current nuclear power plants worldwide. And most $LnO_{1.5}$s are their major fission products (FPs) during irradiation. So, this finding has prompted a hot debate among concerned researchers as to which is radiation-tolerant, the P or F [18–20]. This has also revived interest in the formerly known peculiar second conductivity maximum at $y = 0.50$ in the $Zr_{1-y}Gd_yO_{2-y/2}$ system, i.e., at the most highly ordered ideal P structure shown in Fig. 1c [21–24]. These unique properties of this system have directed our more deliberate attention to the ordered P–disordered DF phase and structure relationships in these SZs. Indeed, some of such P-type local structure evidences of the "disordered" SZ phases are first obtained in this system [1,2,25].

Though a few earlier ND and XRD results seem to support the dopant $[Ln^{3+}(Ca^{2+})]$-defect(V_O) complex model [5,26,27], accumulating more recent structure results [1–3,25] suggest in reverse an intermediate P-based local structure of the "disordered" DF-type SZ phases. Yet, as seen in Table 1, even their several results [1,3,28,29] obtained by the same EXAFS technique (which is supposed to be a novel element-specific SOR X-ray probe best-fit for such local structure study), appear far from mutually consistent. More detailed discussion of reported phase and structure data of these systems will be made later together with the present results.

Table 1 Some representative EXAFS results on several SZs.

Authors (ref.) (nr.)	Systems	Main conclusion
T. Uehara et al. (SSI, 23 (1987) 331) (1)	$GdO_{1.5}$–ZrO_2 ($y = 0.20$–0.50)	Gd^{3+}: CN = 8 constant, Zr^{4+}: CN decreases from 8 to 6, P-type local structure for all.
Tuller, et al. (JSSC, 69 (1987 153) (28)	$YO_{1.5}$–ZrO_2 ($y = 0.1, 0.33, 0.57, 0.67$)	Cation–anion distance: ~ the same as those of the pure systems (2.16 Å for ZrO_2 and 2.38 Å for $YO_{1.5}$). Y network is much more sensitive to the Y/Zr substitution.
Cole et al. (JPCS, 51 (1990) 507) (29)	$LnO_{1.5}$–ZrO_2 (Ln = La, Gd, Er) (5 mol % Ln)	For smaller Er^{3+}, V_O locates close to the host Zr^{4+}. For larger La^{3+}, V_O locates in the proximity of the dopant cation.
Komyoji et al. (SSI, 50 (1992) 291) (3)	$YbO_{1.5}$–ZrO_2 ($0.18 < y < 0.50$) $Ln_2Zr_2O_7$ (Ln = Tb, Dy, Ho, Er, Yb)	In all the systems, Ln and Zr are oxygen 8- and 6-fold coordinated, respectively, suggesting the presence of P-type local structure.

We have attempted to resolve such complicated current status of basic-property studies on SZs using different approaches: These consist of the following three main linked studies including each core result obtained:

(1) The proposal of a new concise a_0 model [30] for remarkably non-Vegardian behavior of these DF oxides so far neither well recognized nor well modeled. This model can describe well such non-Vegardian behavior as V_O effect. In addition, this reveals in SZ(SH)s the presence of a broad a_0 hump over the extended stabilized cubic-DF region, macroscopically signaling the onset of most plausibly the P-type structural ordering over there.

Mainly aiming at identifying what really exists behind this a_0 hump in SZ(SH)s in a global scope of these DF oxides, we have performed: (2) A systematic ^{151}Eu-Mössbauer study of the $M_{1-y}Eu_yO_{2-y/2}$ systems (M^{4+} = Hf, Zr, Ce, U, Th; Ln^{3+} = Eu) covering the wide M^{4+} ionic-radii range from the smallest r_c(VIII) = 0.083 (Hf) and 0.084 (Zr) to 0.105 (Th^{4+}) nm [31a–f]. (Here, Shannon's ionic radii are used [32].) Much smaller ionic radii of Hf^{4+} and Zr^{4+} explain the need for the larger $Ln^{3+}(Ca^{2+})$ F sta-

bilizer and the tendency for the P-type ordering. The Eu^{3+} isomer shift (IS) data exhibiting characteristic V-shaped minima around the ideal-P area ($y \sim 0.50$) were obtained here both for the SZ and SH, verifying their P-type local structure.

Finally, focusing on some specific system both of basic and practical interest, we have performed: (3) a ^{155}Gd-Mössbauer study of the $Zr_{1-y}Gd_yO_{2-y/2}$ system with high radiation tolerance and intriguing ionic-conduction property [33a–d]. The unique recoil-free γ-ray resonance-absorption (Mössbauer) property of ^{155}Gd nucleus has provided us with rich Mössbauer data [IS, quadrupole splitting (QS), line-width, peak height, and relative absorption area (RAA), etc.], revealing many salient features of its P-DF phase and structure relationships.

Most of these results are already reported in the above-cited papers for each study (or system). They are here first thoroughly discussed from a global viewpoint and supplemented with some new considerations and data analyses. To our knowledge, 2 and 3 are the first systematic applications of Ln (^{151}Eu, ^{155}Gd)-Mössbauer spectroscopy for the defect(V_O)- and local structure study of these systems, and, coupled with their PXRD-obtained, average-structure (a_0 and phase) data, demonstrate their unmatched capability as unique microscopic probe for clarifying their multilateral local structure features. All of these results are discussed with reported basic properties of these systems, to promote our understanding of these systems.

MACROSCOPIC LATTICE-PARAMETER STUDY

New crystal-chemical lattice-parameter representation for the DF oxides

We first describe a new concise crystal-chemical a_0 representation applicable for these DF oxides $M_{1-y}Ln_yO_{2-y/2}$ formerly proposed by two of us (Otobe and Nakamura) in a SOFC Proceedings volume [30]. Due to its limited circulation, this model does not seem to be well appreciated even among researchers of this and related areas. To our knowledge, in only one recent paper [34] other than our own, this is actually applied for the a_0 data analysis of ThO_2-$YO_{1.5}$ system, giving good agreement. Since this model appears to have superior practical applicability to any other proposed model [35–38], we intend to describe it again here, including some new considerations and data analyses, to acquire wider recognition and utilization (and even criticism).

Lattice parameter (a_0) of the DF oxides is not only the indispensable prerequisite data for their preparation, but also one of the most important basic macroscopic (bulk) parameters, which largely determines their various key properties such as ionic conductivity and phase stability, etc. It is therefore of prime value to develop a reliable theoretical and/or calculation model, microscopic or empirical, that can properly describe the variations of their a_0s with reasonable accuracy. In usual simple cubic solid solutions (ss) between isomorphic systems, e.g., in the parent F-type $M_{1-y}M'_yO_2$,Vegard's law [the linear a_0(ss) vs. composition (y) relationship] is in most cases a good enough first approximation. Only in extreme cases, such as Cu-Au alloy wherein the a_0 difference between the end members is very large ($\Delta a_0 \sim 0.046$ nm), one needs to go to the higher approximation, e.g., Zen relationship [39,40] assuming linear variation of molar volume ($\propto a_0^3$) (instead of a_0 itself) with y (the ideal solution model with no excess molar volume). However, no such simple cubic oxide solid solutions seem to be known. In some complex oxides, such as the spinel-type $CoGa_xAl_{2-x}O_4$ ($0 \le y \le 2.0$) [41], strongly non-random cation distribution occurs between the tetrahedral (CN = 4) and octahedral (CN = 6) sites; this is reported to cause an appreciable negative deviation from Vegard's law that cannot be accounted for by Zen relationship.

This is indeed true for the parent F-type $M_{1-y}M'_yO_2$ with any M-M' pair (M, M' = Ce, Th, U, Np, and Pu): That is, for all the 10 near-complete solid solutions, Vegard's law is almost strictly obeyed over the entire $0 \le y \le 1.0$. It suffices to cite one example, ThO_2–CeO_2 system with the largest M^{4+} = Th—the smallest M'^{4+} = Ce(Pu) pair [42]. CeO_{2-x} is a surrogate of PuO_{2-x} due to their well-known chemical similarities; their similar ionic radii, $r_c[Ce^{4+}(Pu^{4+})] = 0.097(0.096)$ nm, and their common easily re-

ducible nature, $Ce^{4+}(Pu^{4+}) \rightarrow Ce^{3+}(Pu^{3+})$. Even if much smaller non-F (monoclinic) M'^{4+} = Zr and Hf are added here, the situation is basically unaltered as to their a_0(ss): They generally form two separate solid solutions, the DF-type on the MO_2-rich side and the tetragonal-type on the $M'O_2$-rich side. For example, in $M_{1-y}Zr_yO_2$ (M^{4+} = Ce, U, Th; M'^{4+} = Zr) at T ~ 1500 °C, the former DF-type solid-solution regions steadily narrow from y ~ 0.50–0.60 for M^{4+} = Ce, ~0.4 for U, to ~0.1–0.2 for Th with increase in the ionic-radii difference Δr_c(M-M'). Yet, inside each homogeneity range, the a_0(ss) is reported to follow nearly Vegard's law [42–45]. One striking finding here is; when ThO_2–ZrO_2 powder mixtures with the largest Δr_c(M-M') (see Fig. 4a) were melted above 3000 °C and quenched, their room-temperature XRD analysis shows the formation of a relatively wide DF-type single-phase region for ~0.16 ≤ y ≤ ~0.50, wherein the a_0(ss) almost exactly follows Vegard's law, linearly connecting the a_0 (= 0.560 nm) of pure ThO_2 with that of the "hypothetical" F-type pure ZrO_2; a_0(F-ZrO_2) = 0.510 nm [45]. This is a remarkable result in view not only of the fact that the end members' a_0 difference here (Δa_0 ~ 0.05 nm) is even greater than that of the above Cu–Ag alloy (Δa_0 ~ 0.046 nm) but also of their extremely meta- or un-stable nature to readily decompose into the above two phase mixtures by heating at and below 2000 °C.

In contrast, in the present DF oxides, substitutions of $LnO_{1.5}$ for MO_2 inevitably introduce a fixed large amount of V_O into the anion sublattice; $M_{1-y}Ln_yO_{2-y/2}V_{Oy/2}$. The gross mutual solubility of structurally very similar F-type MO_2 (Fig. 1a) and its superstructure, the C-type $LnO_{1.5}$ (Fig. 1b), together with quite a wide span of covered r_c ratios of these constituent cations, $r_C(Ln^{3+})/r_C(M^{4+})$, makes these DF oxides particularly suitable (and almost only one probable set of) systems for examining how the a_0s of grossly defective solid solutions change with the cation- and oxygen compositions, the r_c of the constituent cations, etc., and how one can successfully model their behavior.

In subsequent several figures, a_0(ss) data of over 10 DF oxides are compiled: Figs. 2a–c show a_0 vs. y plot for three of the larger M^{4+} = Th and Ce systems [46–49], for each one of the smaller M^{4+} = Zr and Hf systems [50–52], and for YSZ reported by many groups [26,53–57], respectively. In addition, Figs. 4a and 7a show those for $M_{1-y}Eu_yO_{2-y/2}$ (M^{4+} = Hf, Zr, Ce, U, Th) and for $Zr_{1-y}Gd_yO_{2-y/2}$ obtained in our study described later, respectively. Throughout these figures, for the two types of superstructure, the C-type $LnO_{1.5}$ (Fig. 1b) and pyrochlore $Ln_2Zr(Hf)_2O_7$ (Fig. 1c), and further for their solid solution phases, all with a_0s double of that of the parent F structure, 1/2 of their a_0s are plotted to compare with those of the DF phase. Also included are calculated a_0 vs. y curves by the two representative models, Kim's [35] and the present model [30].

It is clearly seen in these figures that a_0 data of these systems exhibit quite diverse but systematic variations depending on the r_c of the respective constituent cations (M^{4+}, Ln^{3+}) and their various combinations. Their essential feature distinctively different from the parent F-type $M_{1-y}M'_yO_2$ is remarkably non-Vegardian (nonlinear) character found for all of them: For the larger M^{4+} = Th and Ce systems (Figs. 2a and 4a), the deviation is markedly positive, while for the smaller M^{4+} = Zr and Hf systems (Figs. 2b,c, 4a, and 7a), this is even slightly negative. In addition, the latter show a broad a_0 hump over the extended middle composition range (~0.3 < y < ~0.6–0.7) either for the P-forming (Ln = Eu, Gd) or non-P-forming (Ln = Dy, Er, Y) systems. It is also clear that our model can describe fairly well the reported a_0 data for all of them systematically over the entire 0 ≤ y ≤ 1.0. While Kim's model [35] is only applicable at most for y < ~0.20–0.30, as intended: At y > ~0.30, his model starts to deviate significantly from the reported a_0 data, due to his adopted linear (in y) approximation.

In view of the above near-strict Vegardian behavior of the parent F-type (oxygen-stoichiometric) solid solutions $M_{1-y}M'_yO_2$, such remarkably non-Vegardian character of their oxygen-deficit DF counterparts $M_{1-y}Ln_yO_{2-y/2}$ is definitely due to the presence of fixed large amount of oxygen vacancies ($[V_O] = y/4$) introduced into the anion sublattice by these substitutions ($M^{4+} \rightarrow Ln^{3+}$), i.e., V_O effect. Whether these V_Os are randomly distributed or short-range ordered (as would be the case for the "disordered" DF-type solid solution) or long-range ordered (as in the C-type solid solution), seems to have only minor (or nearly no) effect on their a_0s. Indeed, as seen in Fig. 4a, in CeO_2-$EuO_{1.5}$ system in which

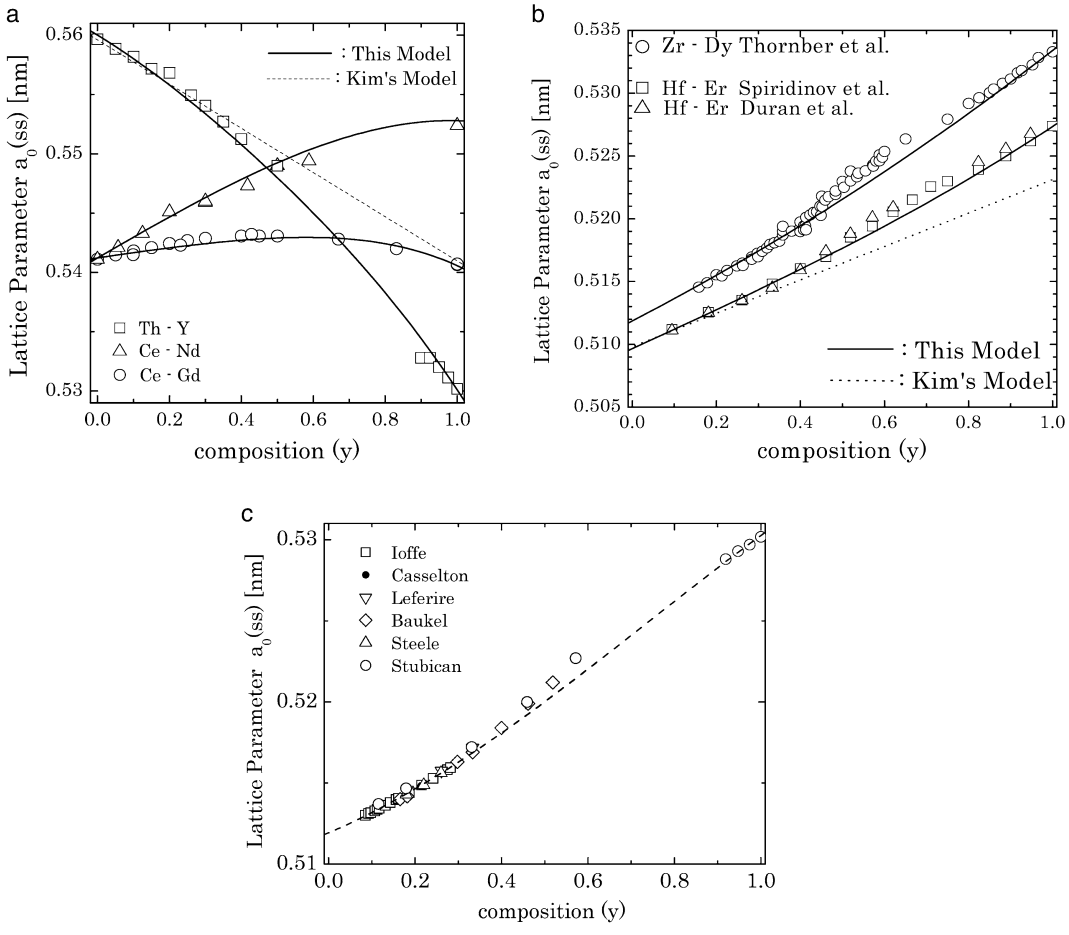

Fig. 2 (a) a_0(ss)(nm) vs. y plot for several M^{4+} = Ce and Th systems. (b) a_0(ss)(nm) vs. y plot for each one M^{4+} = Zr and Hf systems. (c) a_0(ss)(nm) vs. y plot for YSZ system.

the a_0 mismatch between the end members is minimal, nearly complete solid solution is formed over the entire $0 \leq y \leq 1.0$, changing at $y \sim 0.625$ smoothly from the V_O-disordered DF to the V_O-ordered C-type without discernible miscibility gap and a_0(ss) discontinuity in between.

Thus, the core task of any a_0 modeling attempt is to reproduce such remarkably non-Vegardian a_0(ss) data (either positive or negative) in a consistent and quantitative manner, properly incorporating this prime-important V_O effect into the model. To achieve this, different from Kim's approach, we adopt the interpolation method, first fixing the a_0 of either end member, MO_2 ($y = 0$) and $LnO_{1.5}$ ($y = 1.0$), by each experimental value. The main problem is then reduced to devising an appropriate way to connect them, across the solid solution range ($0 < y < 1.0$). In the present model, this almost automatically follows from this first a_0 fixing process for either end member.

To evaluate as precisely as possible the a_0 values of either end member over each wide stability range, their available experimental data have been extensively surveyed and compiled. The main source is the Joint Committee on Powder Diffraction Standards (JCPD) powder diffraction file [58] for $LnO_{1.5}$ and mostly MO_2, and in addition [59] for the actinide (An) dioxides AnO_2. The results are shown in Fig. 3a for either system as a_0(F) (for MO_2) or a_0(C)/2 (for $LnO_{1.5}$) vs. r_c of each cation, $r_c(M^{4+})$(VIII) or $r_c(Ln^{3+})$(VI) each at CN = 8 or CN = 6 as their common abscissa. For pure (monoclinic) ZrO_2 and HfO_2, the most reasonable extrapolation of each a_0(ss) data in the stabilized cubic-DF region ($y >$

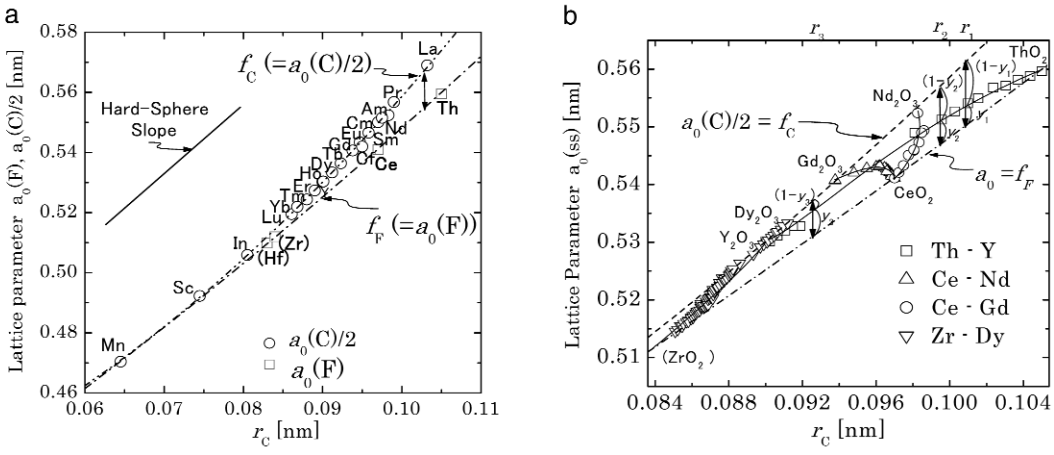

Fig. 3 (a) Lattice parameter of the fluorite-type MO_2 [a_0(F)] and one-half of lattice parameter of the C-type $LnO_{1.5}$ [a_0(C)/2)] plotted against each cationic ionic radii, $r_c(M^{4+})$(VIII) and $r_c(Ln^{3+})$(VI). f_F and f_C: lattice-parameter functionals for a_0(F) and a_0(C)/2 given by eqs. 1 and 2, respectively. The slope (= 4/√3) of the hard-sphere (ion-packing) model (eq. 3) is also shown. (b) Lattice parameter [a_0(ss)] vs. the average cation ionic radius [r_C(ss)] plot for several systems shown in Figs. 2a,b to illustrate the schematic a_0(ss) path across from the MO_2 (y = 0) to the C-type $LnO_{1.5}$ (y = 1.0).

~0.10–0.16) to each y = 0 has been made in Figs. 2b,c, 4a, and 7a, resulting in a_0(F) = 0.512 nm for ZrO_2 and 0.5095 nm for HfO_2. The least-squares fit of these a_0(F) data, including also those of several other AnO_2 (An^{4+} = U, Pu, Np, Am, Cm, and Bk) [59] (not shown in this figure for clarity) gives

$$f_F = a_0(F) = 0.3572 + 1.48\ r_c + 4.3\ r_c^2\ \text{(nm) (at CN = 8)} \quad (1)$$

and for a_0(C)/2 of the C-type $LnO_{1.5}$ (total 20 in number);

$$f_C = a_0(C)/2 = 0.40693 + 0.03741\ r_c + 14.7973\ r_c^2\ \text{(nm) (at CN = 6)} \quad (2)$$

In eqs. 1–2, as shown in Fig. 3a, a_0(F) and a_0(C)/2 are redefined as f_F and f_C, respectively, to use them as the respective a_0 functionals.

On the other hand, according to the hard-sphere (ion-packing) model [6,38], a_0(F) of MO_2 is expressed as

$$a_0(F) = (4/\sqrt{3})\cdot(r_C + r_{O^{2-}}) \quad (3)$$

where $r_{O^{2-}}$ is the ionic radius of oxide ion (O^{2-}) (= 0.138 nm) [32] at CN = 4 in the fluorite lattice. In Fig. 3a, for MO_2, a_0(F) data and its functional (f_F) (eq. 1), though slightly concave, nearly coincide with this ion-packing curve, eq. 3. For the C-type $LnO_{1.5}$, a_0(C)/2 data and its functional (f_C) (eq. 2) exhibit increasing positive deviation from these F curves with increase in r_C(VI) (the inequality $f_C > f_F$ always holds). Plausible origin for such behavior is that, compared with the parent F-type MO_2 having regular oxygen-cube with stronger M^{4+}–O^{2-} bond (CN = 8) (Fig. 1a), the $2V_O$-containing C-type $LnO_{1.5}$ with electrostatic looser (weaker) Ln^{3+}–O^{2-} bond (CN = 6) is apparently more open and defective, and therefore also much more flexible. In fact, the C-type $LnO_{1.5}$ has two kinds of largely and differently distorted octahedral cation sites (CN = 6) (Fig. 1b). At smaller r_C range below ~0.08 nm, f_C approaches to f_F, i.e., the C-type structure approaches to the F structure, though here the actual F-type MO_2 does not exist any more. Yet, some C-type $MO_{1.5}$ (Ln = In, Sc, Mn) do still exist here, demonstrating its much more flexible nature having much wider stability region than the former. With increasing r_C above ~0.08 nm, such distortion and dilation (lattice expansion) from the F structure are accelerated. These

seem to be what are occurring in Fig. 3a for the $2V_O$-containing C-type $LnO_{1.5}$, i.e., the essence of V_O effect.

The length of the perpendicular straight line connecting in between the two a_0 functionals ($f_C > f_F$) at some constant r_C in Fig. 3a, $\Delta f(C–F) = f_C - f_F$, is the a_0 difference between the $2V_O$-containing C-type phase (CN = 6) and the parent F-type phase (CN = 8) at the same r_c, i.e., the full dilation of the lattice by the full $2V_O$ introduction at this r_c. Supposing the solid solution $M_{1-y}Ln_yO_{2-y/2}$ with CN = 8 – 2y on this r_c line, one can reasonably approximate that the introduction of $2y \cdot V_O$ (i.e., from CN = 8 to 8 – 2y) in the $M_{1-y}Ln_yO_{2-y/2}$ on this r_c line brings about the proportional increase ($2y/2 = y$) of its lattice parameter, $y \cdot \Delta f(C–F)$ from the f_F. Thus, the lattice parameter of this solid solution is reasonably calculated as; $a_0(ss)(y) = f_F + y \cdot \Delta f(C - F) = f_F + y \cdot (f_C - f_F) = (1 - y) \cdot f_F + y \cdot f_C$. That is, one reaches a simple conclusion given by

$$a_0(ss)(y) = (1 - y) \cdot f_F + y \cdot f_C \text{ (at CN} = 8 - 2y) \quad (4)$$

Equation 4 means that the lattice parameter $a_0(ss)$ of this solid solution $M_{1-y}Ln_yO_{2-y/2}$ [$= (1 - y) \cdot MO_2 + y \cdot LnO_{1.5}$] is given as the arithmetic composition (y)-average of those (f_F and f_C) of the "hypothetical" two end members at this $r_C(ss)$. Here, the average cationic radius of the solid solution, $r_C(ss)$, is again given by

$$r_C(ss) = (1 - y) \cdot r_M{}^{4+} + y \cdot r_{Ln}{}^{3+} \text{ (at CN} = 8 - 2y) \quad (5)$$

as the arithmetic composition (y)-average of those of the two constituent cations (M^{4+}, Ln^{3+}), $r_M{}^{4+}$ and $r_{Ln}{}^{3+}$. The value of $r_C(ss)$ can be easily calculated from Shannon's r_c data of these cations reported as a function of CN [32]. For example, for $ThO_2–YO_{1.5}$ system (M^{4+} = Th, Ln^{3+} = Y), each Shannon's data can be well approximated by the following equation for ~4 ≤ CN ≤ ~10

$$r_{Th}{}^{4+} = 0.105 + 0.00488 \cdot (CN - 8) - 0.00023 \cdot (CN - 8)^2 \text{ (nm)} \quad (6)$$

$$r_Y{}^{3+} = 0.1014 + 0.00553 \cdot (CN - 8) - 0.00035 \cdot (CN - 8)^2 + 0.00022 \cdot (CN - 8)^3 \text{ (nm)} \quad (7)$$

In combination of the above equations, one can numerically calculate the a_0 (ss)(y) vs. y curves as a function of y (and CN = 8 – 2y) over the entire solid solution range $0 \le y \le 1.0$

Equations 4 and 5 consist of one set of equations which give the full description of the lattice parameter $a_0(ss)(y)$ of the DF oxides $M_{1-y}Ln_yO_{2-y/2}$. The prime-important V_O effect is here readily incorporated into the model through the crystal-chemical a_0(F,C) vs. r_C representation shown in Fig. 3a. We can regard these two equations as an extended version and/or a generalization of the conventional Vegard's law for the isomorphic (and iso-compositional) binary systems [e.g., the F-type $M_{1-y}M'_yO_2$; $a_0(ss) = (1 - y) \cdot a_0(MO_2) + y \cdot a_0(M'O_2)$] to the present DF-type non-isocompositional (oxygen-non-stoichiometric) binary systems. The essential difference between them is that, in Vegard's law, $a_0(ss)$ is the arithmetic composition (y)-average directly of those of the actual two end members (MO_2 and $M'O_2$), while, in the present generalized form (eq. 4), this is that of the a_0 functionals (f_F and f_C) of the two "hypothetical" end members at the same $r_c(ss)$. It is easily shown that in the limit of no V_O effect (i.e., in case that $f_C = f_F$), this generalized form is reduced to the conventional Vegard's law (or its like expression).

In Fig. 3b, in an expanded scale for the concerned region, we have illustrated the schematic application process of this model to several specific DF oxides. This was explained in detail in [30] for $ThO_2–YO_{1.5}$ system [$= (1 - y) \cdot ThO_2 + y \cdot YO_{1.5} = Th_{1-y}Y_yO_{2-y/2}$] having the widest a_0 span between the MO_2 and $LnO_{1.5}$. Referring to Fig. 3b, this is briefly summarized as follows (including some explanatory remarks in each parenthesis):

1. Calculate the average cation radius $r_C(ss)$ of the solid solution $M_{1-y}Ln_yO_{2-y/2}$ using eq. 5, by inserting Shannon's ionic radii data of the constituent cations (M^{4+}, Ln^{3+}), e.g., eqs. 6 and 7. This fixes the position of the system in the abscissa axis.

2. Draw the perpendicular line at this r_C(ss) in between the $f_F(r_C)$ and $f_C(r_C)$. [The lower intersect of this line, $f_F(r_C)$ (eq. 1), is a_0(F) of the "hypothetical" F end member, if the system were CN = 8. Likewise, the upper intercept, $f_C(r_C)$ (eq. 2), is a_0(C)/2 of the "hypothetical" C-type end member, if the system were CN = 6. The actual system is CN = 8 – 2y as a random mixture of these two "hypothetical" end members existing in composition ratio of (1 – y):y.]
3. Internally divide this line by the composition ratio; (1 – y):y, according to eq. 4. The obtained point gives the lattice parameter a_0(ss)(y) of this solid solution. (It is equivalent to say; "make the arithmetic composition (y) average of $f_F(r_C)$ and $f_C(r_C)$ on this line", as expressed above.)
4. Repeat the above process for the whole y range ($0 < y < 1.0$) (e.g., $y = y_1, y_2, y_3, \ldots$, as shown for $Th_{1-y}Y_yO_{2-y/2}$), and obtain the complete a_0(ss) vs. r_C(ss) curve, as depicted for several systems.
5. Convert the obtained a_0(ss) vs. r_C(ss) curve to the usual a_0(ss) vs. y curve to compare with its experimental a_0(ss) data.

The calculated a_0(ss) vs. y curves thus obtained are drawn in these figures for many DF oxides. For the larger M^{4+} = Ce and Th systems (Figs. 2a and 4a), these all describe very well their experimental marked-positive deviation from Vegard's law over the entire $0 \le y \le 1.0$ within scatter of the reported a_0 data. Only the M^{4+} = U system (UO_2–$EuO_{1.5}$) in Fig 4a shows significantly different behavior from those of the other systems. This is due to the occurrence of $U^{4+} \rightarrow U^{5+}$ oxidation, and will be discussed in detail in the next section. As for the smaller M^{4+} = Zr and Hf systems, these also describe fairly well the observed even "reversed' slightly negative deviation from Vegard's law for the widely nonstoichiometric SZ- and SH-type DF phases for y > ~0.10–0.20, at least for the three non-P-forming SZs and SHs (each two and one in Figs. 2b,c), and for the P-forming each one Eu-SZ and Eu-SH in Fig. 4a and one Gd-SZ in Fig. 7a. These results verify the basic validity of the present model, i.e., the way to incorporate the prime-importance V_O effect.

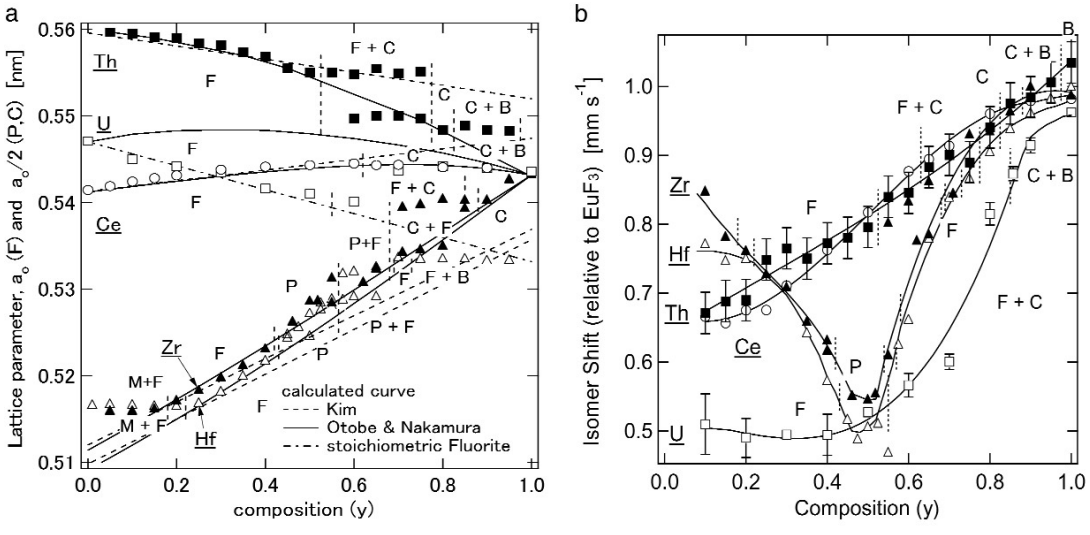

Fig. 4 (a) Phase diagram of MO_2–$EuO_{1.5}$ systems, $M_{1-y}Eu_yO_{2-y/2}$ (M^{4+} = Hf, Zr, Ce, U, Th) expressed as a_0 vs. y plots: F: defect-fluorite (DF) type, C: the C-type, P: pyrochlore type, B: the B-type. Calculated a_0(ss) curves according to the present and Kim's models are also drawn. (b). IS(Eu^{3+}) vs. y plot for MO_2–$EuO_{1.5}$ systems, $M_{1-y}Eu_yO_{2-y/2}$ (M^{4+} = Hf, Zr, Ce, Th, U): Lines are guides for the eye.

In the smaller M^{4+} = Zr and Hf systems, however, as is apparent in these figures, commonly for all the systems, we observe a broad a_0(ss) hump still positively deviating from the calculated a_0 vs. y

curves over the extended middle composition region (~0.30 < y < ~0.60–0.70). This seems to be so either for the non-P-forming Dy- and Y-SZs and Er-SH in Figs. 2b,c or for the P-forming Eu-SZ and Eu-SH in Fig. 4a and Gd-SZ in Fig. 7a. In analogy to the above-cited spinel-type non-Vegardian $CoGa_xAl_{2-x}O_4$ ($0 \le x \le 2.0$) due to the strongly non-random cation distribution [41], this is most plausibly judged to signal that the extensive P-type ordering involving both the cations (M^{4+}, Ln^{3+}) and anions (O^{2-}, V_O) is occurring over there, which cannot be properly accounted for by the present basically "random mixture" model between the F-type MO_2 and the C-type $LnO_{1.5}$. Since the PXRD long-range ordered P-type phase region is generally limited at most to the much narrower ~0.45 ≤ y ≤ ~0.55 range (see Figs. 4a and 7a), this implies that such short-range P-type ordering would be deeply penetrating into the outer apparently "disordered" DF-type SZ (SH) phase region on either side, as suggested by some EXAFS, single-crystal XRD, and Raman studies of SZs [1–3,5].

The fact that this broad a_0 hump is also observed almost equally for the non-P-forming relatively smaller Ln^{3+}(= Dy,Y)-SZs and Er-SH in Figs. 2b,c suggests that even in those systems the short-range P-type ordering is occurring to a similar extent, if even no long-range ordered P phase is formed at y ~ 0.50. This seems to be quite probable by the following reasons:

1. The condition for the P-DF relative stability boundary at around Ln^{3+} = Tb-Gd in SZs(SHs) defined by the cation-radii ratio, Rr_{cr}(P-DF) = $r_C[Ln^{3+}(VIII)]/r_C[Zr(Hf)^{4+}(VI)]$, is estimated to be 1.444~1.463 (1.465~1.483). However, for the larger B^{4+} = Pb(0.0775 nm) [cf. Zr(0.072 nm) and Hf(0.071 nm) at the same CN = 6], one finds several pyrochlores with even smaller Rr_{cr}(P-DF) values than the above; for the A^{3+} = Pr-Gd, $Ln_2Pb_2O_7$ have Rr_{cr}(P-DF) = 1.453–1.368, the latter being the smallest [9]. While the Rr_{cr}(P-DF) values of several non-P-forming smaller Y-, Yb-, Lu-, In-, and Sc-SZs are 1.415, 1.368 and 1.357, 1.278 and 1.208, respectively. Thus, according to this criterion for the Gd-Pb pyrochlore, Y and Yb, i.e., all the Ln = La-Yb except for the smallest (last) Lu, can be P-forming, and only the smallest three, Lu, In, and Sc remain to be non-P-forming. (See Fig. 3a).
2. The P-DF order–disorder transition temperature (T_{tr}) of the ideal (stoichiometric) $Ln_2Zr_2O_7$ (y = 0.50) is reported to decrease with decreasing ionic radii of the Ln^{3+} [60]; for Ln = La, Sm and Gd, T_{tr} = 2300, 2000, and 1530 °C, respectively. So, for the Ln = Y and Yb much smaller than Gd, their T_{tr}s would be quite low well below ~1000 °C. This would kinetically hinder the long-range P-type ordering due to the low mobility of these cations in SZs(SHs).

The above arguments 1–2 indicate that the majority of Ln-SZs(SHs) except for the smallest three Ln = Lu, In, and Sc possibly have microscopically the short-range ordered P-type structure over the extended region of apparently "disordered" DF-type stabilized phases. It is inferred that this possibility manifests itself in the macroscopic broad a_0 hump in SZs(SHs). To identify what really exists behind this new finding (i.e., whether this indeed signifies the P-type ordering or not) constitutes the main theme of the next two Ln-Mössbauer studies on SZ(SH)s and related DF oxides.

This in turn casts a challenge to the present (and any) a_0 modeling attempt of the DF (and any other) oxides of interest; how one can successfully elaborate the model to incorporate properly such strong structural ordering effect. One may extract one key hint for this from the present analysis: Similarly to the a_0 relationship between the ordered and distorted C-type $LnO_{1.5}$ (Fig. 1b) and the parent F-type MO_2 (Fig. 1a) that $a_0(C)/2 > a_0(F)$ in Fig. 3a, the similar inequality, $a_0(P)/2 > a_0(F)$, would hold for the ordered and distorted P-type $Ln_2Zr(Hf)_2O_7$ (Fig. 1c). This would be also true (probably to a lesser extent) for the off-stoichiometric DP-type or even short-range ordered DF-type phases. A clear manifestation of this is supposed to be the observed broad a_0 hump behavior of SZ(SH)s. The elaboration of the present model along this line is now in progress and will be described in a separate paper, including more thorough survey and compilation of a_0(ss) data of these M^{4+} = Hf, Zr, Ce, U, and Th systems.

MICROSCOPIC MÖSSBAUER STUDY

It was shown in the above that the proposed new crystal-chemical a_0(ss) vs. r_C(ss) representation (Figs. 3a,b) can give almost a complete description of remarkably non-Vegardian character of these DF oxides, by taking into account directly the prime-important V_O effect. This has also revealed the presence of a broad a_0 hump over the extended SZ(SH)-type DF phases (~0.30 < y < ~0.70). As discussed there, this a_0 hump in SZ(SH)s is most plausibly judged to be a macroscopic signal for the onset of extensive P-type ordering, in line with their several EXAFS (and other) results [1–3]. However, as seen in Table 1, the latter results seem to be somewhat problematic and inconclusive often inconsistent with one another. To resolve such confusing situation and identify what really exists behind this new finding in SZ(SH)s with different approach, we have adopted Ln-Mössbauer spectroscopy, and performed a systematic ^{151}Eu-Mössbauer study on a series of these DF oxides $M_{1-y}Eu_yO_{2-y/2}$ (M^{4+} = Hf, Zr, Ce, U, Th) and a ^{155}Gd-Mössbauer study specifically on the $Zr_{1-y}Gd_yO_{2-y/2}$. We first mention "Mössbauer spectroscopy" minimum necessary for the present discussions.

Mössbauer spectroscopy is a well-established microscopic nuclear probe for investigating the ionic and electronic structure in the vicinity of the Mössbauer nuclei in solid compounds utilizing their unique recoil-free (recoil-less) γ-ray resonance absorption (Mössbauer) effect [61a–d]. Not to mention, ^{57}Fe Mössbauer nucleus with low-energy ^{57}Co γ-ray source (~14 KeV; measurable up to over 1000 °C) is the most widely and commonly used due to its many superior Mössbauer properties; for example, its IS, the center of gravity of Mössbauer spectrum and a measure of s-electron density at the Mössbauer-nucleus position (Fermi's zero-contact interaction), varies sensitively with the valence (+2, +3, +4, etc.) and spin (high, intermediate, or low) states of Fe in the compounds. In addition, this has very sharp well-resolved quadrupole and magnetic splittings (QS and MS, respectively) due to the high-energy resolution and the large hyperfine-coupling constant.

All the Lns except for Ce have Mössbauer nuclei, and many Ln compounds have been investigated using ^{151}Eu, ^{155}Gd, ^{161}Dy, ^{166}Er, and ^{170}Yb, etc. Among them, only ^{151}Eu-Mössbauer spectroscopy has commercial ^{151}Sm source (1.85 GBq in the present case) with relatively low γ-ray energy (~21.5 KeV: measurable up to ~800 °C). So far, Ln-Mössbauer spectroscopy has hardly been applied for the complex defect(V_O)- and local structure study of these DF oxides containing Lns as their major constituents, in spite of their intensive study by varieties of other spectroscopic methods as mentioned above. We could find only one paper on ^{151}Eu-Mössbauer study of the similar Bi_2O_3-Eu_2O_3 system with several different Bi/Eu ratios reported by Battle et al. [62].

Hitherto, only the ideal pyrochlores often appearing at the center of such DF oxides at y = 0.50 used to be the target of Ln-Mössbauer study [8]. This is plausibly because they have defect(V_O)-free crystallographic well-defined characteristic axial-anisotropic Ln-O configuration (CN = 8) with two short apical and six more-distant oxygens (Fig. 1c), best fit for investigating the QS behavior. Chien and Sleight [63] have made systematic ^{151}Eu-Mössbauer study on Eu-pyrochlores $Eu_2M_2O_7$ (M = Hf, Zr, Pt, Pb, Mo, Sn, Ru, Ir, Ti) including the present M^{4+} = Zr and Hf, and reported on the structure (a_0, Eu–O bond length and anisotropy) vs. ^{151}Eu-Mössbauer parameters [IS(Eu^{3+}), QS] correlations. But, until now, we are not aware of any subsequent extension of such ^{151}Eu-Mössbauer study to the DP ($y \neq 0.50$) and the more-outer DF-phases for any of those $Eu_2M_2O_7$. Instead, there are many Ln-Mössbauer studies on non-Zr(Hf) pyrochlores performed in connection with the so-called Goldanskii–Karyagin (GK) effect [61a] (asymmetric QS caused by lattice-vibration anisotropy) in $^{156}Gd_2Ti_2O_7$, $^{151,153}Eu_2Ti_2O_7$, $^{154}Gd_2Ti_2O_7$, and $^{155}Gd_2$(Ti, Sn, Ru, Ir, etc.)$_2O_7$, and $^{170}Yb_2Ti_2O_7$ [64a–d]. (See also [8].) Such Ln-Mössbauer studies have been mostly done for systems with much smaller B-site cations than the present Zr and Hf, for the axial Ln-O anisotropy, so the QS and GK effect are much stronger in those systems. Only in [64c], it is briefly mentioned that "in either $^{155}Gd_2Zr_2O_7$ or $^{155}Gd_2Hf_2O_7$ no GK effect was observed, giving only very broad Mössbauer spectra, probably because of the existence of oxygen vacancies (V_Os) which were distributed random throughout the lattice", suggesting the "significantly disordered" nature of these Gd-Zr and Gd-Hf pyrochlores

present at around the P-DF stability boundary region. However, as seen later, our present ^{155}Gd-Mössbauer study on the $Zr_{1-y}Gd_yO_{2-y/2}$ system performed in detail over the whole composition range ($0.05 \le y \le 1.0$) will reveal many new intriguing features of ordered P–disordered DF phase and structural relationships in this system that cannot be represented by such short remark.

^{151}Eu-Mössbauer and PXRD study of the $M_{1-y}Eu_yO_{2-y/2}$ system (M^{4+} = Hf, Zr, Ce, U, Th; Ln^{3+} = Eu)

In this coupled ^{151}Eu-Mössbauer and PXRD study [31a–f], we have attempted to clarify the controversial P-DF local structure in the M^{4+} = Zr and Hf systems in a global scope of these DF oxides covering the wide $r_c(M^{4+})$ range [32]; r_c(VIII) = 0.083(Hf) → 0.084(Zr) → 0.097(Ce^{4+}) → 0.100(U^{4+}) → 0.105(Th^{4+}) nm. For the details of their experiments and data analyses, see the above-cited papers. We only note here that room temperature ^{151}Eu-Mössbauer measurements give almost symmetric (for the parent F-based M^{4+} = Th, Ce, and U systems) or slightly asymmetric and broader (for the SZ and SH) single-line Mössbauer spectrum, and its peak Doppler velocity (mm/sec) gives the Eu^{3+}-isomer shift [IS(Eu^{3+})] relative to that of EuF_3 (the reference). It is well known that in oxides IS(Eu^{3+}) correlates with the average Eu–O bond length (and CN) that shorter the Eu–O bond length (smaller the CN) larger the IS(Eu^{3+}) [65]. We make use of this near-linear IS(Eu^{3+}) vs. Eu–O bond length correlation (see Fig. 5b), and intend to refine it with the present results. To derive the QS data is possible for some largely distorted SZ(SH)s around $y \sim 0.50$ [31f], but this is hardly possible for the less-distorted majorities. So, discussion here is confined to the IS(Eu^{3+}) data.

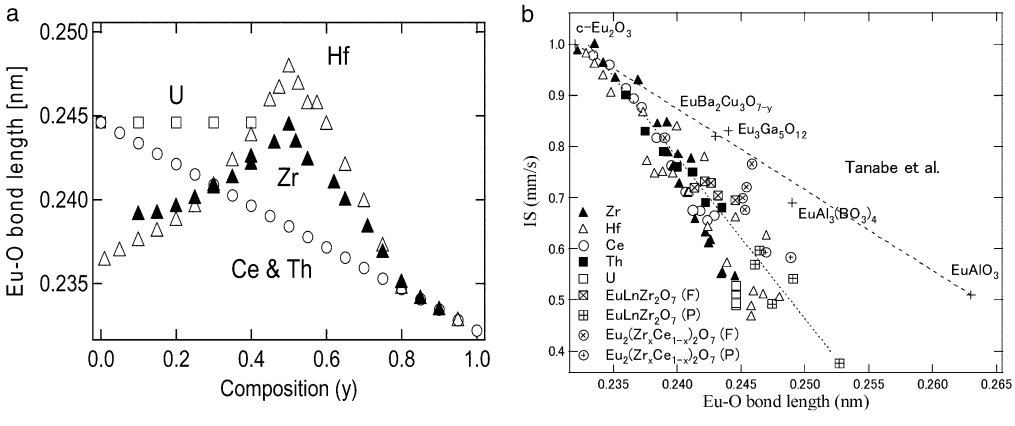

Fig. 5 (a) The average Eu–O bond length vs. y plot for MO_2–$EuO_{1.5}$ systems, $M_{1-y}Eu_y O_{2-y/2}$ (M^{4+} = Hf, Zr, Ce, U, Th). (b) IS(Eu^{3+}) vs. average Eu–O bond length plot for the MO_2–$EuO_{1.5}$ systems, $M_{1-y}Eu_yO_{2-y/2}$ (M^{4+} = Hf, Zr, Ce, U, Th) and for several other oxides reported by Tanabe et al. [65]. Some data for $Eu_2(Ce_{1-x}Zr_x)_2O_7$ and $EuLnZr_2O_7$ [31f] are also included here. Lines are guides for the eye.

Figures 4a and b summarize in pair the macroscopic PXRD phase-diagram and the microscopic ^{151}Eu-Mössbauer IS(Eu^{3+}) data for all these systems, respectively. In Fig. 4b, at a glance, the characteristic V-shaped IS(Eu^{3+}) minima around the ideal-P area ($y \sim 0.5$) both for the Eu-SZ and Eu-SH, in sharp contrast to those of the parent F-based M^{4+} = Ce, U, and Th systems, seems enough to convince us of their intermediate P-based local structure. It is also obvious that among the three F-based systems, M^{4+} = U system has different behavior from M^{4+} = Ce and Th systems. So, we first discuss them separately as (1) M^{4+} = Ce and Th; (2) U; and (3) Zr and Hf, using as each guideline the present a_0(ss) model in Fig. 4a and the IS(Eu^{3+}) vs. Eu–O bond length correlation in Fig. 4b.

M^{4+} = Ce and Th: The parent F-based DF-type solid solution

From the characteristic convex a_0 behavior following well the calculated DF-type a_0(ss) vs. y curve in Fig. 4a (solid line) and almost linearly increasing IS(Eu^{3+}) vs. y curve in Fig. 4b for both systems, we can regard them as a naïve parent F-based DF-type solid solution continuously formed from each pure MO_2 (M^{4+} = Ce, Th) at $y = 0$. According to the IS(Eu^{3+}) vs. Eu–O bond length correlation, this near-linear increase of IS(Eu^{3+}) with y means that the average Eu–O bond length (and CN) of the system is almost linearly decreasing with y. This agrees with the present a_0 model where the CN decreases on an average according to CN = 8 – 2y (the MO_2-$LnO_{1.5}$ random mixture model), and therefore due to the decrease of repulsion between the decreasing number of coordinating oxide ions (O^{2-}s), the average Eu–O bond length decreases with y. The average Eu–O bond lengths for the both systems were calculated using Shannon's $r_C(Eu^{3+})$ data given as a function of CN (= 8 – 2y) [and $r(O^{2-})$(IV) = 0.138 nm at CN = 4 in the F lattice; Fig. 1a] [32]. The results are shown in Fig. 5a, and indeed show a near-linear decrease with y. In Fig. 4b, the IS(Eu^{3+}) data of the M^{4+} = Ce system exhibit somewhat different sigmoid shape from those of the Th system. However, in view of the estimated experimental uncertainty of these IS(Eu^{3+}) data depicted for the latter, both sets of data are here assumed to be the same. This is striking in view of the relatively large difference in their a_0(ss) in Fig. 4a, and in turn seems to rationalize the above Eu–O bond-length calculation common to both systems.

As for some phase-diagram details in Fig. 4a, reflecting the lattice-mismatch difference between these two systems, as mentioned formerly, CeO_2-$EuO_{1.5}$ system (the best lattice-matched among the five systems) forms almost a complete solid solution, changing smoothly from the V_O-disordered DF to the V_O-ordered C-type at y ~ 0.625. While the Th^{4+}-counterpart (relatively largely lattice-mismatched) forms the DF-type solid solution only up to y ~ 0.50, and, traversing a wide miscibility gap, a narrow C-type phase appears at around y ~ 0.80, and finally the B-type $EuO_{1.5}$ at $y = 1.0$. The thermodynamically stable high-temperature form of pure $EuO_{1.5}$ above 800 °C is the B-type structure (CN ~ 7), and hence this is not stabilized to the C-type, unlike the CeO_2 case. The present phase diagram for ThO_2-$EuO_{1.5}$ system generally agrees with that reported by Keller et al. for T = 1700 °C [66]. In conclusion, in both of these parent F-based larger M^{4+} (= Ce, Th) systems, it is likely that a naive DF-type solid solution basically with random cation (M^{4+}, Eu^{3+}) and anion (O^{2-}, V_O) distribution in each sublattice is formed. This is evidenced both by the macroscopic phase-diagram (Fig. 4a) and microscopic Mössbauer data (Fig. 4b), i.e., in good agreement of their a_0 data with the present DF-type a_0 model in Fig. 4a and their IS(Eu^{3+}) data consistent with this DF-type random solid solution model (CN = 8 – 2y). Weak DF → C-type ordering only of V_O does not seem to affect much the both properties of these systems.

M^{4+} = U: The oxygen-stoichiometric F-type solid solution (y < ~0.50)

The formation of oxygen-stoichiometric F-type solid solution by partial oxidation of U^{4+} to U^{5+}, i.e., $U^{4+}{}_{1-2y}U^{5+}{}_{y}Eu^{3+}{}_{y}O^{2-}{}_{2}$ in detailed chemical formula, is readily known from the both experimental results: In Fig. 4a, experimental a_0(ss) data only of this system almost linearly decrease with y up to y ~ 0.50, markedly deviating from the DF-type a_0 vs. y curve (solid line). They follow well the F-type curve, f_F for MO_2 (eq. 1 in Fig. 3a) (dash-dot curve); this curve was calculated using Shannon's r_c data [32] for each cation (at CN = 8) in the above chemical formula. And in Fig. 4b, this system takes nearly a constant (smallest) IS(Eu^{3+}) for y < ~0.50, almost equal to those of the ideal P of the Eu-SH at around y ~ 0.50, where the larger A^{3+} (= Eu^{3+}) is oxygen eight-fold coordinated [CN(Eu^{3+}) = 8] (Fig. 1c). This means that in this system Eu^{3+}, U^{4+}, and U^{5+} are all CN = 8 for y < ~0.5, since the system is oxidized up to the F-type dioxide composition. At $y = 0.50$, all the U^{4+} in this system is oxidized to U^{5+}; $U^{5+}{}_{0.5}Eu^{3+}{}_{0.5}O_2$. For y > ~0.5, the system showed complex heterogeneous nature, and hence was not investigated in detail. The calculated Eu^{3+}(VIII)–O bond length, constant for 0 < y < ~0.50 and the same as that for the above M^{4+} = Th and Ce systems at $y = 0$ (0.1066 + 0.138 = 0.2446 nm), is plotted in Fig. 5a up to $y = 0.40$.

Some additional remarks on such different behavior of urania(UO_2)-based solid solution are appropriate: In other four systems (M^{4+} = Hf, Zr, Ce, Th) with the stable M^{4+} valence in air, their solid solutions are easily prepared by the usual ceramic method using the initial $MO_2 + EuO_{1.5}$ powder mixtures and heating them several times at ~1500 °C in air. In urania(UO_2)-based systems, however, due to its thermodynamic very stable nature (its very sluggish reaction with other oxides) [67], we cannot generally use pure (stoichiometric) UO_2 as the starting material. Instead, we usually use the higher uranium oxide U_3O_8 (stable in air and much more reactive) mixed with $EuO_{1.5}$ (or with another oxides), and react them at 1000 to 1500 °C, simultaneously rising the heating temperature and changing the atmosphere from air, inert He to hydrogen (H_2), successively in several steps. After confirming the formation of homogeneous solid solution, the reduction to the oxygen-deficit DF-type solid solution $U_{1-y}Eu_yO_{2-y/2}$ is performed at ~1500 °C under H_2 atmosphere. Similar process (the initial solid-solution formation in an oxidative and/or inert atmosphere and its subsequent reduction to the oxygen-deficit composition in reducing atmosphere) is favorably used for the industrial fabrication of MOX [$U(Pu)O_{2-x}$] fuel to avoid the remaining of inhomogeneous Pu-rich region (Pu spot). Accordingly, the observation of oxygen-stoichiometric solid solution in this study is not caused by the sample preparation process. This is rather judged to have occurred during the handling (pulverization and packing) process of the prepared oxygen-deficit samples at room temperature in air for the present PXRD and Mössbauer experiments. Such easy oxidation of oxygen-deficit urania solid solutions to near-stoichiometric composition in air even at room temperature is additional cumbersome problem, especially in dealing with their powder samples [68].

M^{4+} = Zr and Hf: The intermediate P-based stabilized solid solution

The a_0 data of these two stabilized cubic-DF systems, Eu-SZ and its Hf-analog, Eu-SH, in Fig. 4a, show that, in contrast to the above parent F-based larger M^{4+} = Ce, U, and Th systems, both exhibit even a slightly negative non-Vegardian behavior rising up to the a_0 of the C-type $EuO_{1.5}$ at $y = 1.0$, similarly to other SZs and SHs shown in Figs. 2b,c and 7a. Their a_0(ss) data are also well reproduced by the present DF-type a_0 model. However, it appears that either here similar broad a_0 hump exists over the extended SZ (SH)-type cubic DF phase region for ~0.3 < y < ~0.7 for the both, though their higher y region (~0.55 < y < ~0.70) is mostly the two-phase region. In these systems, apart from pure ZrO_2(HfO_2) at $y = 0$, the four single-phase regions exist with increasing y: first, the stabilized cubic DF phase for ~0.16 ≤ y < ~0.45 (somewhat narrower ~0.22 ≤ y < ~0.45 for the latter); second, the ordered P phase with limited DP-type homogeneity range for ~0.45 ≤ y ≤ ~0.55 (almost the same for the both); third, the second very narrow DF-type phase around y ~ 0.70; and fourth, the stabilized C-type phase for ~0.85 ≤ y ≤ 1.0 for the SZ (the B-type $EuO_{1.5}$ at $y = 1.0$ for the SH). Only the first DF/P phase boundary is continuous, and the other two at higher-y regions [P/DF/C(B)] are separated by each wide miscibility gap. Thus, given their overall similarities, as in the larger M^{4+} = Ce vs. Th case, either in this smaller Hf vs. Zr case, the slight difference in their lattice-mismatch with $EuO_{1.5}$ gives rise to some phase-diagram difference: The B-type $EuO_{1.5}$ is here too stabilized into the C-type solid solution for the larger Zr^{4+}, but not for the smaller Hf^{4+}.

With this knowledge on their phase diagrams, their very similar characteristic IS(Eu^{3+}) data exhibiting sharp V-shaped minima around the ideal P-area (y ~ 0.50) in Fig. 4b make a sharp contrast to any of the parent F-based M^{4+} = Ce, Th, or U systems. These data highlight the present Eu-Mössbauer study, and seem to give a clear-cut answer to the controversy on the local structure of the "disordered" DF-type stabilized phases in SZs(SHs): In a word, these are decisively the intermediate P-based one: The IS(Eu^{3+}) data both of Eu-SZ and Eu-SH are neither constant (CN ~ 8) as in the M^{4+} = U system nor increasing steadily with y (CN = 8 – 2y) as in the Ce and Th systems: Strikingly, they both initially decrease sharply inside the "XRD-disordered" stabilized cubic-DF phase region (~0.20 ≤ y < ~0.45), and attain the minima around the narrow P-phase region (~0.45 ≤ y ≤ ~0.55). This initial sharp decrease of IS(Eu^{3+}) with y indicates that this "disordered" stabilized DF phase (~0.20 ≤ y < ~0.45) is by no

means the parent F-based naïve DF-type one (CN = 8 – 2y) as in the M^{4+} = Th and Ce systems, but definitively the intermediate P-based short-range ordered one.

As shown in the above a_0(ss) analysis, in the lower ~0.20 ≤ y ≤ ~0.30 region, a_0(ss) data of these SZs(SHs) either follow well the present DF-type a_0 curve. This may be interpreted that in this lowest-y region these systems have predominantly DF-type near-random structure as in the M^{4+} = Ce and Th systems. However, even here, IS(Eu^{3+}) data of the present Eu-SZ(SH) decrease with increasing y, opposite to those of the latter. In turn, for y > 0.55, both the IS(Eu^{3+}) data even more sharply increase with y until they reach those of the latter at around y ~ 0.80–0.85. This is reasonable because here both the systems shift from the largest CN(Eu^{3+}) = 8 in the ideal P at y = 0.5 to CN = 6 (or 7) at y = 1.0 for the C- (or the B-) type structure twice as rapidly as that in the M^{4+} = Ce and Th systems: In the latter, this occurs according to CN = 8 – 2y (from CN = 8 at y = 0 to 6 at y = 1.0), using the whole 0 ≤ y ≤ 1.0 range.

The V-shaped minima in the ideal-P structure at y ~ 0.50 with the largest CN(Eu^{3+}) = 8 for the A^{3+} cation (= Eu) (Fig. 1c) means that both the systems have the respective longest average Eu–O bond length at y = 0.50. In the pyrochlore structure shown in Fig. 1c, the larger A^{3+} (= Eu) locates at the center of distorted cube (CN = 8) composed of two apical oxygens (O2 at 8a site) at the cube corner of the parent F lattice and six more-distant oxygens (O1 at 48f site) shifted from this cubic corner. So, to fully describe the structure, in addition to the lattice parameter a_0(P) [= 2·a_0(F)], we need one more additional parameter, oxygen positional parameter (x') for O1, which defines its shift (3/8 – x') from the cube corner position (x' = 3/8 = 0.375 for the parent F structure) [8,9]. Using these two parameters, each Eu–O bond length is calculated by

$$d_{A\text{-}O(8a)} = \left(\sqrt{3}/8\right) a_0 \tag{8}$$

$$d_{A\text{-}O(48f)} = \left[\frac{1}{32} + \left(\frac{1}{2} - x'\right)^2\right]^{\frac{1}{2}} a_0 \tag{9}$$

From the structure refinement of the PXRD pattern for each ideal P composition (y = 0.50), we obtain the following values of a_0(P) and x' (those of Chein and Sleight [63] are also given in each parenthesis); for $Eu_2Zr_2O_7$ a_0(P) = 1.0588(1.0588) nm and x' = 0.343(0.344), and for $Eu_2Hf_2O_7$ a_0(P) = 1.05456(1.056) nm and x' = 0.336(0.343). Inserting these values of a_0(P) and x' into eqs. 8 and 9, we obtain for the overall average Eu–O bond length [= (2·$d_{A\text{-}O(8a)}$+ 6·$d_{A\text{-}O(48f)}$)/8] for each system; 0.245(0.250) nm for $Eu_2Zr_2O_7$ and 0.248(0.2454) nm for $Eu_2Hf_2O_7$.

As is clearly seen in Fig. 4b, experimental IS(Eu^{3+}) data of the smaller M^{4+} = Hf system are systematically smaller than those of the larger Zr system throughout the measured entire 0.1 ≤ y ≤ 1.0: That is, the more-distorted smaller M^{4+}(= Hf) system has inversely "the longer" average Eu–O bond length than the less-distorted larger-M^{4+}(= Zr) system, while the average lattice parameter a_0(ss) itself is certainly larger in the larger-M^{4+}(= Zr) system in Fig. 4a. This noteworthy result is consistent with the above argument in our a_0 analysis that the more-distorted system (Hf) tends to be locally more expanded (dilated) than the less-distorted system (Zr). This is correctly reflected in the above-calculated values of the average Eu–O bond length at y = 0.50 of our own for both systems; 0.248(Hf) > 0.245(Zr) nm, but not in Chien and Sleight's results; 0.2454(Hf) < 0.250(Zr) nm. So, when the former our Eu–O bond-length values at y = 0.50 are plotted for the both systems in Fig. 5a, they are indeed found to be the longest; in the Hf system this is even distinctively longer than that of the parent F-based Ce, Th, and U systems at y = 0; the afore-calculated same value (= 0.2446 nm) at the same CN = 8.

The most straightforward reasonable interpretation for such V-shaped IS(Eu^{3+}) behavior with minima at y = 0.5, also having consistently the smaller IS(Eu^{3+}) (the longer average Eu–O bond length) in the smaller Hf system than in the larger Zr system, is that, with increasing y in the apparently "dis-

ordered" DF-type stabilized phase (~0.20 ≤ y < ~0.45), the P-type local distortion (anisotropy) of the system and hence the local lattice distortion and expansion around the larger A^{3+}(= Eu) are rapidly growing, i.e., its average Eu–O bond lengths are steeply becoming longer, until the system attains the most distorted, the most expanded, and anisotropic ideal P-type structure at y = 0.50 (Fig. 1c) with the longest average Eu–O bond. In another scenario (e.g., some DF-type or other "disordered" average-structure model), it seems difficult to rationalize the occurrence of such systematically "inversed" longer average Eu–O bond length in the smaller-Hf^{4+} system over the entire 0.10 ≤ y ≤1.0.

Thus, assuming the short-range ordered P structure for the "disordered" stabilized DF phase for ~0.20 ≤ y < ~0.45 and also for ~0.55 < y ≤ ~0.85 [though the latter is in fact mostly the P/DF/C(B) two-phase region except for a very narrow DF phase around y ~ 0.70], the most consistent sets of average Eu–O bond length were calculated for the both systems, and the results are shown in Fig. 5a. A sharp hill-top (inverse-V) shape behavior with maxima at y ~ 0.50 is obtained for the average Eu–O bond length in the either system. Their derivation process is briefly as follows.

As seen in Fig. 4b, the IS(Eu^{3+}) data of both systems cross with those of the parent F-based Ce and Th systems at y ~ 0.25–0.30 for the lower-y side and at y ~ 0.80–0.85 for the higher-y side: That is, at these compositions, both systems have the same (known) average Eu–O bond lengths as the latter. For the lower-y side, as seen in Fig. 5a, we have set this composition at y = 0.3 for the Ce system, instead of y = 0.25 for the Th system. (This choice of either y = 0.3 or 0.25 makes only minor difference in the calculated Eu–O bond length for both.) In this lower-y region, a constant CN(Eu^{3+}) = 8 was assumed, for the system has both the Zr(Hf)- and oxygen-excess compositions; i.e., the excess Zr partly fills also the A-site (CN = 8) and the excess oxygen occupies the 8b V_O site in Fig. 1c, as expressed by the following P-type chemical formula; $[(Eu,Zr)_2]_A[Zr_2]_BO_6O_{1+x}$ (x > 0). On this assumption, at y = 0.3, using the known average Eu–O bond length [from that of the M^{4+} = Ce(Th) system in Fig. 5a] and the double of their experimental a_0 [$2 \cdot a_0(F) = a_0(P)$], we can calculate the oxygen positional parameters (x') of the both systems from eqs. 8 and 9.

While, for the Eu-excess and oxygen-deficit higher-y region (~0.50 < y ≤ ~0.80–0.85), additional complexities of the system should be taken into account; first, the appearance of the B-site Eu and the CN change of the A-site Eu according to the P-type chemical formula here; $[Eu_2]_A[(Eu,Zr)_2]_BO_6O_{1-x}$ (x > 0): Here, the excess V_O (= x) is assumed to occupy the apical (minor) O2 site, for in another case of introducing this into the major O1 site, the B-site Eu and Zr become even less than oxygen six-fold coordinated (CN < 6) in Fig. 1c. Second, in both systems, the IS(Eu^{3+})-crossing point here (y = ~0.80–0.85) actually locates inside the two-phase region for both systems (Fig 4a). The more adequate choice would be y = 0.70 where they both really have the apparently "disordered" narrow DF phase. However, either choice does not make much difference in the resultant (calculated) average Eu–O bond lengths either here. So, for convenience, we have set y = 0.80 as the IS(Eu^{3+})-crossing point for the "hypothetical" short-range ordered P phase for the both systems.

The trend of the obtained x' values of the both systems from the ideal P composition (y = 0.50) is:

For Eu-SZ: 0.343 (at y = 0.30) ← x' = 0.343 (at y = 0.50) → 0.363 (at y = 0.80).

For Eu-SH: 0.346 (at y = 0.30) ← x' = 0.336 (at y = 0.50) → 0.361 (at y = 0.80).

These results indicate that, when the system departs from y = 0.50, except for x' = 0.343 at y = 0.30 for the Eu-SZ, these x' values at y = 0.30 and 0.80 increase significantly toward x' = 0.375 for the parent F-type structure, and thus, as expected, the systems are moving to the less-ordered and less-distorted P-type structure. Assuming the linear variation of x' for the either region (0.30 ≤ y ≤ 0.50 or 0.50 ≤ y ≤ 0.80) and using the experimental lattice-parameter a_0(P) [= $2 \cdot a_0$(F)] data, the average Eu–O bond lengths are calculated from eqs. 8 and 9 for the both systems, as shown in Fig. 5a. For the lower-y region, the same calculation was extended down to the smaller y → 0.10 range.

As shortly mentioned above, in this lowest-y DF region (~0.20 ≤ y ≤ ~0.30) for which the present DF-type a_0(ss) model applies well, it is also conceivable that SZ(SH)s indeed have the "disordered" DF-type phase rather than the short-range ordered P-type phase. However, so far as the present IS(Eu^{3+})

data are concerned, it seems more probable that even here this and many other SZ(SH)s have a P-like (not necessarily the P-type) local structure, the degree and mode of which changing at around $y \sim 0.30$. Corresponding well to the behavior of a_0(ss) data that start to deviate toward the broad hump at $y \sim 0.30$, the IS(Eu^{3+}) data of these Eu-SZ and Eu-SH exhibit a weak but apparent slope change to the steeper one at $y \sim 0.30$ in Fig. 4b. The nature of this lowest-y DF phase will be further discussed later in the light of the ^{155}Gd Mössbauer results on the Gd-SZ.

Using Fig. 5a, we can now convert the abscissa of Fig. 4b from the composition (y) to the average Eu–O bond length of the system. The results are shown in Fig. 5b: Contrary to our expectation, all the IS(Eu^{3+}) data for the present five M^{4+} = Hf, Zr, Ce, U, and Th systems are found to give significantly steeper IS(Eu^{3+}) vs. Eu–O bond length relationship than that reported by Tanabe et al. for the perovskite-related several oxide compounds [65]. In this figure, we have also included our recent results of $EuLnZr_2O_7$ (Ln = La-Tm) and $Eu_2(Zr_xCe_{1-x})_2O_7$ solid solution ($0 \le x \le 1.0$) [31f].

Of course, there are several inconsistent parts in our results. For example, in Fig. 5a, the M^{4+} = Ce, Th, and U systems at $y = 0$ (all CN = 8) have the same calculated Eu–O bond length of 0.2446 nm somewhat smaller than (but nearly comparable with) those (0.245 and 0.248) of the ideal pyrochlores $Zr(Hf)_2Eu_2O_7$ at $y = 0.50$ at the same CN = 8. However, as is apparent in Fig. 4b, in reality, the M^{4+} = Ce and Th systems at $y = 0$ alone have significantly higher (extrapolated) IS(Eu^{3+}) values of ~0.65–0.62 mm/sec than those (~0.46–0.56 mm/sec) of the latter three systems at the same CN = 8, i.e., the M^{4+} = U for $y < \sim 0.5$, and the Eu-SZ and Eu-SH at $y \sim 0.50$. An alternative interpretation for this inconsistency is that in the Eu-doped ceria and thoria (M^{4+} = Ce, Th) in such low dopant concentration range ($0 < y < \sim 0.10$) the dopant(Eu^{3+})-defect(V_O) associate (complex) is indeed formed, as often postulated for these systems [5], and hence the CN(Eu^{3+}) is decreased significantly from the supposed 8 to ~7.5–7.0 level. Though conceivable, this possibility is not pursued here further, for this leads to even steeper IS(Eu^{3+}) vs. Eu–O bond length correlation not only in M^{4+} = Ce and Th systems themselves but also in the Eu-SZ and Eu-SH through the above IS(Eu^{3+})-matching process. Another irregularity in the present data in Fig. 4b is that the IS(Eu^{3+}) data of the B-type $EuO_{1.5}$ (CN ~ 7) at $y = 1.0$ for the three M^{4+} = Hf, U, and Th systems scatter around those of the C-type $EuO_{1.5}$ (CN = 6) for the two M^{4+} = Zr and Ce systems, not necessarily following the expected regularity that IS(Eu^{3+}) (B-type; CN ~ 7) < IS(Eu^{3+}) (C-type; CN = 6).

However, far beyond such inconsistency-rooted scatter of our results, Tanabe et al.'s data seem to have too gradual slope, starting from the same C-type $EuO_{1.5}$ (CN = 6). At present, we cannot judge whether these results merely represent the two different IS(Eu^{3+}) vs. Eu–O bond length relationships for the differently structured two classes of oxide materials, the DF- and the perovskite-type, or they have some more significant ground and meaning. This should be clarified in the future.

As one such next-step attempt to pursue more unified description of these IS(Eu^{3+}) data, Fig. 6 shows the IS(Eu^{3+}) vs. bond-valence sum (BVS) plot for the both set of data. According to Brown [69], the BVS of a given central cation is given by

$$\mathrm{BVS} = \sum (r_0 / r)^N \ (r_0 = 0.209 \text{ nm}, N = 6.5 \text{ for } Eu^{3+} \text{ in oxides}) \tag{10}$$

where r_0 and N are empirical numerical parameters for the central cation, and r is the individual Eu–O bond length for which summation over all the coordinating oxygens should be made. The intention of Brown's BVS approach is to evaluate the detailed nature of basically ionic anisotropic chemical bond including the local- as well as crystal-structural distortion effect beyond simplified "average bond-length approximation". Apparently, a better (more unified) description seems to be attained by this approach than in Fig. 5b, both sets of data now being more intermingled with each other. However, at this stage, Fig. 6 is at most a tentative one necessitating more elaboration: Several major problems in the present Fig. 6 are in brief as follows.

1. Only for the ideal P structure at $y = 0.50$ (Fig. 1c), such reasonably accurate individual Eu–O bond-length (r) data to be summated in eq. 10 (here the two kinds given by eqs. 8 and 9) are avail-

able from their XRD structure study. For the off-stoichiometric long- or short-range ordered DP-type phase ($y \neq 0.50$), the situation is not so simple as initially thought. For example, in the case of the Eu-deficit SZ ($y < 0.50$); $[(Eu,Zr)_2]_A[Zr_2]_BO_6O_{1+x}$ ($x > 0$), our calculations show that the BVS obtained for the A-site cation using the above-derived oxygen-positional parameter (x') of O1 in eq. 10 gives (adequately enough) the cation-composition averaged BVS value for the total Eu^{3+}+Zr^{4+} present on the A-site: This naturally increases steadily from ~+3.0 for the Eu^{3+} to ~+4.0 for the Zr^{4+} with decreasing y from 0.50 (i.e., increasing the Eu-deficiency), shifting the resultant IS vs. BVS plot to the right-hand side far beyond the abscissa BVS range in Fig. 6. For this reason, many data points for off-stoichiometric SZ and SH solid solutions (either $y < 0.50$ or $y > 0.50$) shown in Fig. 5b could not be plotted in Fig. 6. This explains the much sparser data points present in Fig. 6 than in Fig. 5b. To extract reliable individual Eu(Zr)–O bond length data in such off-stoichiometric DP systems ($y \neq 0.50$) needs additional consideration, and it is based refined data analysis.

2. For most of the other systems plotted in Fig. 6, including those reported by Tanabe et al., such detailed structure and Eu–O bond data are not available either (or at least are not enough surveyed whether those are available or not). So, for either of those systems, we are obliged to use each average Eu–O bond length (which is readily known from each abscissa value in Fig. 5b) multiplied by each CN in eq. 10, instead of their actual summation over the individual Eu–O bonds, invalidating the original idea of the BVS approach. This is also the case for the parent DF-type "disordered" (random) solid solutions in the M^{4+} = Ce and Th systems because of another reason; the difficulty here is that the cations (Eu^{3+}, Ce^{4+}, and Th^{4+}) in such "disordered" DF-type solid solutions naturally have a different number of V_O-coordinated variously distorted oxygen polyhedral (CN = 8, 7, 6, etc.) with generally different $Eu^{3+}(M^{4+})$–O bond lengths from one another. In spite of intensive studies up to now, the details of Eu–O bond length distribution in such complex defective structure are not known well.

Yet, the tentative results shown in Fig. 6 seem enough to encourage us to possibly make a future attempt of combining Mössbauer IS(Eu^{3+}) (and any other cation's IS) data with the BVS concept of Brown.

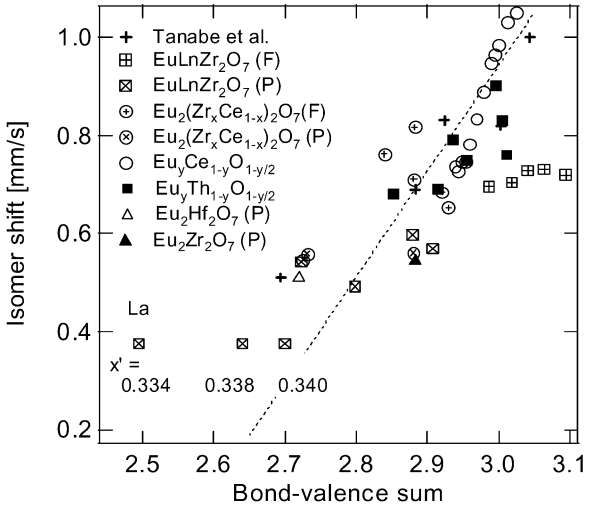

Fig. 6 IS(Eu^{3+}) vs. BVS plots for systems shown in Fig. 5b. Line is a guide for the eye. For $LaEuZr_2O_7$, the three different x' value (= 0.334, 0.338, 0.340) cases are shown to illustrate the resultant difference in BVS calculated in eq. 10.

^{155}Gd-Mössbauer and PXRD study of the $Zr_{1-y}Gd_yO_{2-y/2}$ system

The $Zr_{1-y}Gd_yO_{2-y/2}$ system has many unique properties of basic and practical interest. As mentioned above, this is the only one SZ (and DF)-type oxide-ion conductor which exhibits a second conductivity maximum in the ideal P $Gd_2Zr_2O_7$ at $y = 0.50$ [21–24]. Furthermore, its maximum conductivity is reported to decrease by a factor of ~1/5 by disordering treatment above $T_{tr} = 1530$ °C [70]. The search for P-type oxide-ion conductors in recent years has its main stimulus in such unique conduction properties of this system. Also, the lately found high radiation tolerance of $Gd_2Zr_2O_7$, together with growing nuclear interests in SZs as IMF and nuclear waste form, has aroused a hot debate as to the origin and mechanism of radiation tolerance in these systems, the F vs. P [15–20]. However, as clarified above through the extensive a_0 analysis and the ^{155}Eu-Mössbauer study on these DF oxides, most SZs, with either smaller or larger Ln-stabilizers than Gd, are likely to have the intermediate P-based short- and/or long-range ordered structure much more extensively than thought before. In view of this fact, it seems more reasonable for SZs to discuss this radiation tolerance issue, as well as their many other intriguing properties, not from a simplified "F or P?"-type viewpoint, but based on the more careful considerations on such ordered P–disordered DF hybrid nature of these systems.

On these motivations, to shed new light on their detailed P-DF phase and structure relationships, we have performed coupled PXRD and ^{155}Gd-Mössbauer studies specifically on this system present in the vicinity of P-DF stability boundary region in small composition interval of $\Delta y = 0.05$ or even less. Due to the unique Mössbauer property of ^{155}Gd nucleus different from the above ^{155}Eu nucleus, we were able to obtain rich ^{155}Gd-Mössbauer data such as IS (Fig. 7b), QS (Fig. 7c), line width [Γ(exp)] (Fig. 8a), peak height (ε_0) (Fig. 8b), and relative absorption area [RAA = $\Gamma(\text{exp})\cdot\varepsilon_0$] (Fig. 8c). Some of those data (IS, QS) have been already discussed in several preceding papers [33a–d]. So, briefly mentioning them, we mainly focus here on the latter Γ(exp), ε_0, and RAA data (Figs. 8a–c) for which no detailed analysis has been given before. Since these three parameters represent the shape [Γ(exp) and ε_0] and the magnitude [RAA = $\Gamma(\text{exp})\cdot\varepsilon_0$] of the observed Mössbauer spectrum, they are directly related to the quantity and the physiochemical state of the Mössbauer atom ^{155}Gd in the system, i.e., the Mössbauer absorption thickness (T_A) and hence the recoil-free (recoil-less) fraction (f) of the measured system essential for the observation of the Mössbauer effect:

$$T_A = \sigma\cdot n(^{155}\text{Gd})\cdot f = 21.75\cdot f \tag{11}$$

where σ is the Mössbauer γ-ray absorption cross-section of ^{155}Gd nucleus (= $32.88\cdot10^{-20}$cm^2), and $n(^{155}\text{Gd})$ is the concentration of ^{155}Gd Mössbauer atom in the sample. A constant total Gd concentration, $n = 115$ mg/cm^2 = $4.403\cdot10^{20}$ atom/cm^2, was employed for all the present samples [33,71]. This corresponds to n(^{155}Gd) = $6.52\cdot10^{19}$ atom/cm^2 (the natural abundance; 14.8 %). Inserting these numerical values, the second equality in eq. 11 is obtained.

The presence of recoil-free fraction f (>0) first enables us to observe the Mössbauer effect, i.e., the sharp resonance-absorption of γ-ray from the source by the absorber without recoil of the Mössbauer nucleus (^{155}Gd). This in turn directly reflects the rigidity (stiffness) of the crystal lattice around the ^{155}Gd Mössbauer atom, which is most properly represented by the Debye model, i.e., by the Debye temperature (Θ_D) of the system. Since our ^{155}Gd-Mössbauer measurements are conducted with relatively high γ-ray energy of the ^{155}Eu/^{154}SmPd$_3$ source ($E_\gamma = 86.53$ KeV) at constant $T = 12$ K ($<<\Theta_D$) both for the source and the absorber (= sample), f and Θ_D are interrelated by the following low-temperature approximation [61b,d]:

$$f = \exp[(-E_R/k\Theta_D)\cdot(3/2 + \pi^2T^2/\Theta_D^2)] \ (T << \Theta_D) \tag{12}$$

where $E_R = (1/2M_{(155Gd)})\cdot(E_\gamma/c)^2$ is the recoil energy of the ^{155}Gd nucleus ($M_{(155Gd)}$ is the atomic mass of ^{155}Gd, E_γ is the Mössbauer γ-ray energy, and c is the velocity of the light), k is the Boltzmann constant, and $T = 12$ K. Upon insertion of all these known numerical values into eq. 12, we can calculate Θ_D from f. Its qualitative trend is, of course, the higher the Θ_D, the larger the f, and

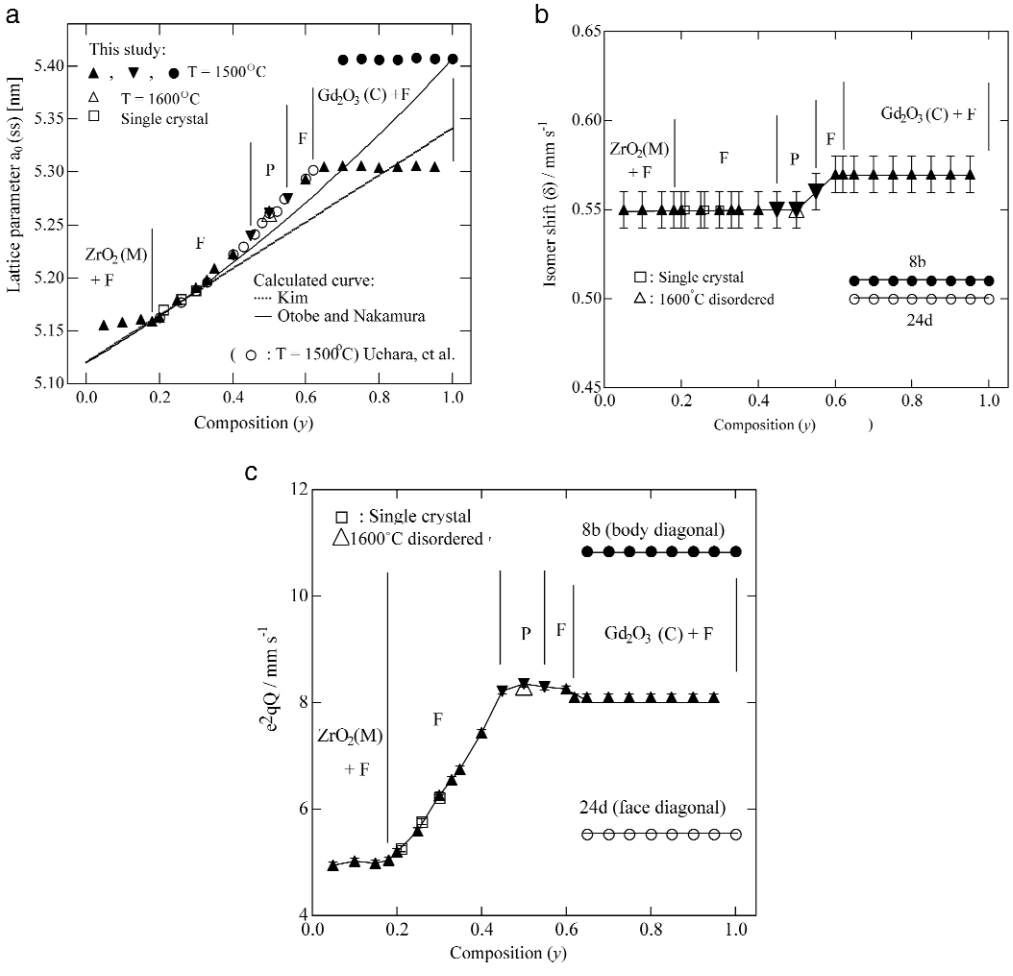

Fig. 7 (a) Phase diagram of ZrO_2–$GdO_{1.5}$ systems, $Zr_{1-y}Gd_yO_{2-y/2}$ expressed as lattice parameter, a_0(ss), vs. composition (y) plot: F: defect-fluorite (DF) type, C: the C-type, P: pyrochlore type. a_0(ss) data reported by Uehara et al. [1] are also included. Calculated curves according to the present and Kim's models are also drawn. (b) IS (Gd^{3+}) vs. composition (y) plot for ZrO_2–$GdO_{1.5}$ systems, $Zr_{1-y}Gd_yO_{2-y/2}$: Line is a guide for the eye. (c) QS (e^2qQ) vs. composition (y) plot for ZrO_2–$GdO_{1.5}$ systems, $Zr_{1-y}Gd_yO_{2-y/2}$: Line is a guide for the eye.

vice versa. From the analysis of these Γ(exp), ε_0 and RAA data, we can derive the f and hence the Θ_D of the system in eq. 12. These f and Θ_D are the most important linked two basic parameters of solid compounds crucial for understanding their various (thermal, thermodynamic, structural, and mechanical) properties. We will return to this central issue later.

Figure 7a first summarizes the XRD phase diagram of this system. Compared with Eu-SZ(SH) in Fig. 4a, this SZ with Ln^{3+} = Gd the next to Eu in the Ln series is much simpler; the intermediate P phase (~0.45 ≤ y ≤ ~0.55) is sandwiched by two "disordered" stabilized DF phases (~0.18 ≤ y < ~0.45 and ~0.55 < y ≤ ~0.62) on either side, and for y > 0.62 the latter coexists with the C-type $GdO_{1.5}$ dissolving almost no ZrO_2 (less than 5 mol %) at ~1500 °C. Similarly to other SZs, the proposed DF-type a_0 model, as well as Kim's model, can describe well the a_0(ss) data for y < ~0.30. Here, we observe a broad a_0 hump over the extended ~0.30 < y < ~0.62 region, positively deviating from the present a_0 vs. y curve. According to Zinkevich et al. [72] who have recently performed detailed PXRD and ED studies on this system in a fine Δy = 0.01–0.02 interval, the single P phase exists for ~0.44 ≤ y ≤ ~0.54 at 1400

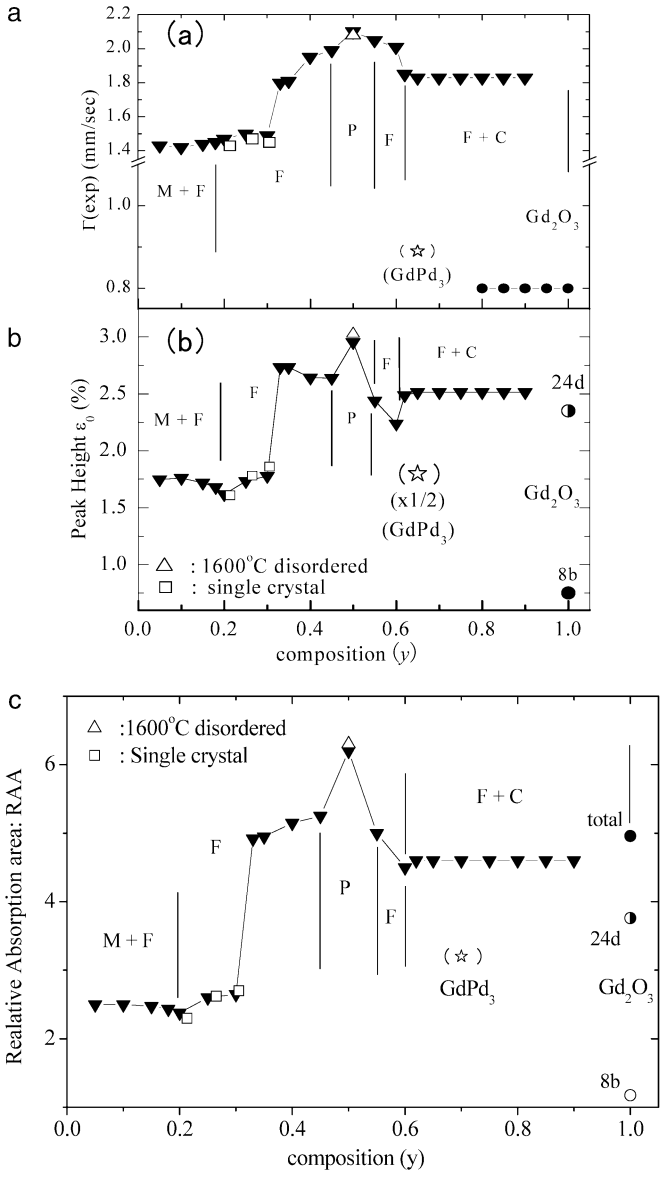

Fig. 8 (a) 2Γ(exp) vs. y plot for ZrO_2–$GdO_{1.5}$ systems, $Zr_{1-y}Gd_yO_{2-y/2}$. Line is a guide to the eye. (b) ε_0 vs. y plot for ZrO_2–$GdO_{1.5}$ systems, $Zr_{1-y}Gd_yO_{2-y/2}$. Line is a guide for the eye. (c) RAA vs. y plot for ZrO_2–$GdO_{1.5}$ systems, $Zr_{1-y}Gd_yO_{2-y/2}$. Line is a guide for the eye.

°C, and the a_0(ss) over the entire SZ phase (~0.18 ≤ y ≤ ~0.62) indeed exhibit non-Vegardian sigmoid variation. Though not so obvious in Fig. 7a, their data reveal the presence of clear a_0 kinks both at y ~ 0.35 and ~0.50, suggesting the onset of macroscopically observable phase and structural changes at these compositions.

As cited above [64c], ^{155}Gd-Mössbauer spectrum of this ideal P $Zr_2Gd_2O_7$ at y = 0.50 is very broad, exhibiting no GK effect. In fact, this is the broadest among all the present systems (Fig. 8a). As is clearly seen in these figures, the present ^{155}Gd-Mössbauer data reveal many salient features of disordered DF–ordered P phase and structure relationships in this SZ. Their most pronounced feature cor-

responding to that of the above Eu-SZ(SH) [the characteristic V-shaped IS(Eu^{3+}) minima at $y \sim 0.50$ in Fig. 4b] is likewise the occurrence of characteristic maxima in all the QS, line-width, peak-height, and RAA data at $y \sim 0.50$ in Figs. 7c to 8a–c throughout. (The IS data in Fig. 7b alone show different upward shift at $y \sim 0.50$.) These data in a word signify that the most strongly and anisotropic Gd–O bonded P structure with the highest Θ_D is formed for the ideal $Zr_2Gd_2O_7$ at $y = 0.50$ (Fig. 1c), and this is spreading out almost over the entire SZ solid solution ($\sim 0.18 \leq y \leq \sim 0.62$), steadily decreasing its P-type anisotropy. Or, more cautiously, the P-type region may exist for $\sim 0.30 < y \leq \sim 0.62$, excluding its lower $\sim 0.18 \leq y \leq \sim 0.30$ range where different "disordered" DF-like character may be suggested in Figs. 8a–c.

First in Fig. 7b, unlike the IS(Eu^{3+}) data (Fig. 4b), the IS(Gd^{3+}) data do not show simple correlation with the average Gd–O bond length, but seem to reflect more sensitively the structural difference in the Gd–O bond between the system. In the Gd-deficit region up to $y = 0.50$, these take nearly a constant value of ~0.55 mm/s characteristic for P oxides [8,33c] considerably larger than either of the 24d or 8b site in the C-type $GdO_{1.5}$ (~0.50–0.51 mm/s). This constant IS(Gd^{3+}) for $y \leq 0.50$ supposedly represents the constant CN ~ 8 of the A-site Gd^{3+} [33a–c]. For $y \geq 0.50$, the IS(Gd^{3+}) exhibits a clear upward-shift to ~0.57 mm/s at $y = 0.62$, corresponding well to the XRD-observed a_0 kink at $y \sim 0.50$ [72]. As in the above Eu-SZ(SH), CN(Gd^{3+}) is supposed to change at $y = 0.50$ from CN ~ 8 to CN < 8 for the oxygen-deficit DP phase, due to the excess V_O introduction into the 8a O2 site. Though, structurally, the system is here likely to approach to the C-type Gd_2O_3 (CN = 6), this upward IS(Gd^{3+}) shift is rather oppositely departing the system more from the latter.

Since the Gd^{3+} ion has well-known spherical $4f^7$ electron configuration (the $^8S_{7/2}$ ground state), as discussed in [33b–c], the QS (= e^2qQ) data in Fig. 7c give direct information on the anisotropy of ionic (both anionic and cationic) configuration around the $^{155}Gd^{3+}$, i.e., the lattice contribution. Its major contribution comes from the 1st NN oxygen coordination. The C-type $GdO_{1.5}$ ($y = 1.0$) gives two well-resolved doublets nearly in 3:1 ratio in RAA in Fig. 8c, in fair agreement with the presence of the two kinds of Gd^{3+} sites, the 24d and 8b sites in 3:1 ratio in Fig. 1b. The minor 8b site with body-diagonal $2V_O$s (the outer-doublet) has significantly more (in fact the most) distorted noncubic oxygen (+ outer ionic) configuration around the Gd^{3+} than the major 24b site with face-diagonal $2V_O$s (the inner doublet). The QS value of the former is nearly twice as large as that of the latter. Such QS behavior of the C-type $GdO_{1.5}$ has been satisfactorily explained by the QS calculation based on the point charge model (PCM) of Barton and Cashion [73] and of our own [33b,c]. (See Fig. 3 in [33c] for the actual ^{155}Gd Mössbauer spectra of these solid solutions.)

For the solid solutions with various y ($\sim 0.18 \leq y \leq \sim 0.62$), it should be first mentioned that their ^{155}Gd Mössbauer spectra consist of very broad single (one) doublet, as shown in Fig. 8a, suggesting the presence of single kind of QS-split distorted (anisotropic) noncubic Gd site with high f and Θ_D. However, as discussed below there is another possibility here that the presence of several kinds of distorted noncubic Gd sites with each different QS splitting gives rise to such "unresolved" very broad single doublet spectrum of the system. Anyway, their QS data exhibit a rapid overall near-continuous increase with y inside the stabilized DF-type "disordered" phase ($\sim 0.18 \leq y < \sim 0.45$) toward the broad maximum around the single P-phase area ($\sim 0.45 \leq y \leq \sim 0.55$). Note that the maximum QS at the ideal P ($y = 0.50$) reaches at most around the middle of those of the either site in the C-type $GdO_{1.5}$, starting from the low (in fact the lowest) QS at the monoclinic/cubic DF phase boundary ($y \sim 0.18$). Such a trend of QS with y has also been reproduced semiquantitatively by our PCM QS calculation based on the P-type structure model (CN = 8) [33b]. In brief, the calculated QS results show that, analogously to the Eu-SZ(SH), this XRD-disordered stabilized DF phase ($\sim 0.18 \leq y < \sim 0.45$) has in fact a rapidly growing P-type short-range order. One can see this here more directly as a steadily increasing QS, i.e., as the steadily increasing anisotropy of the Gd–O bond in Fig. 1c resulting from the steady decrease of oxygen positional parameter (x') of O1 to the minimum $x' = 0.3495$ at $y = 0.50$. (In [33b–c], a different definition of $x' > 0.375$ (for the F-type structure) was adopted. So, this is here redefined to give the present $x' < 0.375$). In this sense, one could regard this Gd-deficit solid solution ($\sim 0.18 \leq y \leq \sim 0.45$) as a

near-continuous switch-over region of the Gd–O bonding character from the parent F-based near-cubic one (Fig. 1a) with small QS to the intermediate P-based strongly axial-anisotropic one with large QS (Fig. 1c), keeping its near-constant CN(Gd^{3+}) ~ 8, consistent with the above IS(Gd^{3+}) interpretation in Fig. 7b.

According to Moriga et al. [2], such microscopic P-type local structure of this Gd-SZ extends over ~0.30–0.35 ≤ y ≤ ~0.62, matching well with the extended a_0 hump region in these SZ(SH)s. Also, the present QS data seem to show a subtle slope change around y ~ 0.30–0.33. Rather surprisingly, as seen in these figures, the disordering treatment of $Zr_2Gd_2O_7$ at ~1600 °C (>T_{tr}) changes neither the QS nor any other ^{155}Gd-Mössbauer parameters to any significant extent, in spite of its obvious XRD average-structure change from the long-range ordered P-type to the disordered DF-type at T_{tr} ~ 1530 °C. This is also in line with Moriga et al.'s view [2,60] that the short-range P-type order is retained also far beyond the apparent macroscopic T_{tr} ~ 1530 °C up to ~1900 °C range at y = 0.50. It is likely that the true disordering to the DF-type near-random (disordered) structure will be attained only by heat treatment above ~1900 °C, as if this would be realized only in the largely Gd-deficit (grossly off-stoichiometric) lowest-y side solid solution phase in the ~0.18 ≤ y ≤ ~0.30 range. Only in this lowest-y region, the proposed DF-type a_0 model can describe well the reported a_0(ss) data of SZs. However, even here, whether this is truly the disordered DF-type structure phase as in doped-cerias and thorias seems dubious, for at least in both the Eu-SZ and Eu-SH (Fig. 4b) the IS(Eu^{3+}) data decease with increasing y, opposite to those of the latter (M^{4+} = Ce, Th).

In contrast, the line width [Γ(exp)] in Fig. 8a and the peak height (ε_0) in Fig. 8b, and their product, the relative absorption area [RAA = Γ(exp)·ε_0] in Fig. 8c, the all exhibit a sharp discontinuous jump in between y = 0.30 and 0.33, and thereafter form each unique bell-shaped maximum around the ideal $Zr_2Gd_2O_7$ (y = 0.5). In short, these data mean that the f and hence the Θ_D of this solid solution increase abruptly in between y = 0.30 and 0.33 and take the maxima at the ideal P structure at y = 0.50 (Fig. 1c). Thus, again here, reinforcing many related findings, we have one other clearest ^{155}Gd-Mössbauer evidence for the onset of drastic local structure and physicochemical property changes of Gd-SZ at y ~ 0.30–0.33. This composition is now almost unambiguously identified as the onset point of collective short-range DF → DP structural ordering of the system toward the macroscopic realization of long-range ordered P structure for ~0.45 ≤ y ≤ ~0.55. Related findings reported in literature are:

1. As mentioned in the foregoing, ionic conductivity of this system changes its trend around this composition from the decreasing to increasing direction toward the second conductivity maximum at y = 0.50 [21]. Though the exact mechanism for this intriguing behavior is still not understood well, it seems certain that this local-structural ordering serves to facilitate the P-type conduction pass for the oxide ions. The next finding mentioned below seems to have close connection with this conduction behavior.
2. The P-type antiphase boundary starts appearing around here in the single-crystal XRD and ED results of this and related SZs [2,60]. This most plausibly suggests that each initially independently nucleated small P-like (not necessarily P-type) microdomains in the lowest-y side DF subphase region (~0.18 ≤ y ≤ ~0.30) have grown up sufficiently both in number and size, and begin to contact and interact with one another around this composition, first forming misaligned and/or displaced P-type antiphase boundaries between them.

In Figs. 8a–c, in addition to those of the C-type $GdO_{1.5}$ (y = 1.0), the respective data for an intermetallic compound $GdPd_3$, isomorphic with the present ^{155}Gd-Mössbauer source, ^{155}Eu/^{154}SmPd_3 prepared by Wang et al. [71], are also included for reference. $GdPd_3$ has the cubic $CuAu_3$-type structure with single kind of isotropic Gd–Pd bond [74], i.e., QS = 0 in this system. So, this system alone has sharp symmetric single Mössbauer spectrum (singlet) [71]. Accordingly, 1/2 of its peak height (ε_0) is plotted in Fig. 8b, to compare with those of the SZ solid solutions (one doublet) and the C-type $GdO_{1.5}$ (two doublets) in the same one (single) doublet condition. Note that in Fig. 8a the line width of

this single spectrum is reasonably narrow [Γ(exp) = 0.89 mm/s], nearly comparable with those of the well-resolved two doublets for the two kinds of Gd^{3+} sites in the C-type $GdO_{1.5}$ (the 24d and 8b sites), Γ(exp) = 0.80 mm/s; the same for the both sites and the narrowest of all the present systems [71].

In sharp contrast to these $GdPd_3$ and the C-type $GdO_{1.5}$, as mentioned briefly above, all the present solid solution has the QS-split single doublet with very broad line width, Γ(exp), in Fig. 8a, superficially suggesting the presence of single kind of distorted (noncubic) Gd^{3+} site with high f and Θ_D. For example, the lowest-y side DF subphase for ~0.18 ≤ y ≤ ~0.30 has the narrowest Γ(exp) = ~1.4–1.5 mm/sec, among all the SZ solid solutions. Yet, even this level of Γ(exp) is already about twice as broad as those of the former. Together with irregular composition (y) variation of ε_0 data in the higher-y side DF solid solution (~0.30 ≤ y ≤ ~0.62) in Fig. 8b, we are obliged to think that, besides the supposed high f and Θ_D of the system, such very broad Γ(exp) of these SZ-type DF solid solutions (~0.18 ≤ y ≤ ~0.62) at least partly arises from the Mössbauer-spectrum distortion, i.e., the extra line width, Γ(exp), broadening in Fig. 8a and the accompanying ε_0 reduction in Fig. 8b, extensively occurring over there. In fact, ε_0 data of these solid solutions in Fig. 8b is not so high as expected from the corresponding Γ(exp) data in Fig. 8a, especially in the lowest-y side ~0.18 ≤ y ≤ ~0.30 region: There, the solid solutions have even slightly (or significantly) lower ε_0 than $GdPd_3$ (or the C-type $GdO_{1.5}$), indicating that the spectrum-distortion [the Γ(exp) broadening and the ε_0 reduction] is indeed occurring.

The most common origin (mechanism) for such extra Γ(exp) broadening (i.e., Mössbauer spectrum distortion) is generally attributed to the "disorder (randomness)" of the system. We have already observed such spectrum distortion in this Gd-SZ between once- and twice-reacted samples at ~1500 °C [33d] where the former less-homogeneous solid solutions were found to have simultaneously the broader Γ(exp) and the lower ε_0 than the latter more-homogeneous one over the entire SZ-phase region (~0.18 ≤ y ≤ ~0.62). Here, reported Γ(exp) and ε_0 data for the solid solutions are all those obtained for the latter twice-reacted samples at ~1500 °C. In these figures, these polycrystalline samples have all the ^{155}Gd-Mössbauer data nearly identical with those of the three crushed-powder samples of high-quality single crystals in the same lowest-y DF subphase area, demonstrating their homogeneous enough nature.

Then, the origin of such Mössbauer-spectrum distortion in Figs. 8a,b in polycrystalline as well as single-crystal samples is judged to be the intrinsic disorder and randomness (microscopic heterogeneity) of these macroscopically homogeneous enough nonstoichiometric solid solutions. The most likely intrinsic disorder here is inferred to be near-random or only short-range ordered coexistence (mixture) of at least several (or even more) kinds of noncubic (distorted) Gd^{3+} sites: In view of predominantly P-based local structure nature of these SZs, their majorities are considered to be variously distorted O8-coordinated Gd^{3+} sites (CN = 8). Due to the DF-P hybrid nature of this system, a small amount of O7- and further O6-coordinated Gd^{3+} sites (CN = 7, 6) might also exist here. Even each Gd^{3+} site with the same CN = 8 (7 or 6) is likely to have various degrees of noncubic distortion (QS splitting) diversified from the near-cubic one (QS ~ 0) in the parent F-type structure (Fig. 1a) to the strongly axial-anisotropic one with large QS in the P-type structure (Fig. 1c), as evidenced in the overall composition (y) dependence of QS in Fig. 7c. And the overlapping of many QS-split individual doublets of such variously distorted noncubic Gd^{3+} sites is supposed to result in such very broad "unresolved" single doublet of these solid solution systems.

This situation might be best illustrated as follows; in the defective but long-range ordered C-type $GdO_{1.5}$, as shown in Fig. 1b, the presence of crystallographic well-defined two kinds of noncubic Gd^{3+} sites with the same CN = 6 (24d and 8b sites) but with largely different local distortion (i.e., largely different QS) in Fig. 7c gives well-resolved two doublets with each narrow line width (Fig. 8a) and peak height with near 3:1 ratio (Fig. 8b). If several (two or three) doublets with their QSs distributed between those of these original two doublets are added there, the resultant Mössbauer spectrum would probably merge into a very broad almost-unresolved composite single doublet. Or, if ever the C-type $GdO_{1.5}$ could be really "disordered" by some means, this might be enough to change their well-resolved two doublets themselves to such very broad unresolved single doublet. Owing to the enhanced DF-P hybrid

nature of this Gd-SZ present in the vicinity of macroscopic DF-P relative stability boundary region, the occurrence of such disorder-induced wide variation and distribution of local P-DF mixed anisotropic Gd-O bonding structure appears conceivable in these widely nonstoichiometric solid solutions.

After all, what we can say on these raw Γ(exp) and ε_0 data in Figs. 8a,b is that, due to the possible simultaneous presence of such various kinds of disordered and distorted noncubic Gd^{3+} sites, considerable ^{155}Gd-Mössbauer spectrum distortion [the simultaneous Γ(exp) broadening and ε_0 reduction] is probably occurring throughout the present solid solution. However, this is an important but only a subfeature of this system. The main feature here is that there is a drastic overall change in the quality (integrity) of crystal-lattice around the Gd^{3+} from basically the disordered DF-type to the short-range ordered P-type at $y \sim 0.30$–0.33, and this gives rise to a discontinuous jump of f and Θ_D of the system and finally leads to the formation of the macroscopic P structure at $y \sim 0.50$ area.

Below, introducing the functional forms of these ^{155}Gd-Mössbauer parameters [Γ(exp), ε_0, and RAA], we make some more quantitative discussion of such Mössbauer-spectrum distortion in this system. Thereupon, on this basis, we attempt to derive the f and Θ_D of all the present systems (eq. 12) using these data. The Γ(exp) and ε_0 of a given ^{155}Gd-Mössbauer spectrum are properly expressed by the next respective equations as a function of Mössbauer absorption thickness (T_A) of ^{155}Gd nucleus given by eq. 11 [61b,d]

$$\Gamma(\text{exp})/2\Gamma = 1 + 0.135\, T_A \ (0 \le T_A \le \sim 5) \tag{13a}$$

$$\Gamma(\text{exp})/2\Gamma = 1.01 + 0.145\, T_A - 0.0025\, T_A^2 \ (\sim 4 \le T_A \le \sim 10) \tag{13b}$$

where 2Γ is the line width of the Mössbauer γ-ray source, ^{155}Eu/^{154}SmPd. In the ideal case, 2Γ is supposed to takes the (limiting) natural width (= 0.475 mm/sec) of (infinitely thin) source. And

$$\varepsilon_0/f_S = 1 - \exp(-T_A/2)\cdot J_0\,(i\, T_A/2) \tag{14}$$

where f_S is the recoil-free fraction ($0 < f_S < 1$) of the same γ-ray source, and J_0 is the 0th-order modified Bessel function (i; the unit of imaginary number). The normalized line width [Γ(exp)/2Γ ≥ 1)] in eqs. 13a,b and the normalized peak height ($0 < \varepsilon_0/f_S < 1$) in eq. 14, both are functions only of the absorption thickness (T_A) and hence of the f of the measured sample (absorber), for $T_A = 21.75\cdot f$ in eq. 11. In short, both are monotonously increasing functions of T_A (and of f) with steadily decreasing slope at larger T_A (and f) range; i.e., the larger the Γ(exp) and ε_0, higher the f of the system, and vice versa.

Equations 13a,b and 14 are only applicable for the "distortion-free" intrinsic Γ(exp) and ε_0 data of the system, which seems to be only the case for the "disorder-free" C-type $GdO_{1.5}$ and $GdPd_3$ in Figs. 8a,b. These equations in short mean that if one system has larger Γ(exp) than the other, this should have also larger ε_0 as well, and vice versa. At a glance, it is easily known in Figs. 8a,b that this consistency requirement is not fulfilled in all the Γ(exp) and ε_0 data for these solid solutions ($\sim 0.18 \le y \le \sim 0.62$): For example, for the higher-y DF $\sim 0.33 \le y \le \sim 0.45$, the ε_0 data in Fig. 8b slightly decrease with increasing y; i.e., it follows in eq. 14 that the f of the system should decrease with y. On the other hand, since the corresponding Γ(exp) data in Fig. 8a exhibit more-natural increasing trend with y in the same region, it follows in eqs. 13a,b that f increases with y, contradicting with the above result. More globally, in comparison with the C-type $GdO_{1.5}$ and $GdPd_3$ (in the same single-doublet condition), for all the higher-y SZ solid solutions over $\sim 0.33 \le y \le \sim 0.62$, their Γ(exp) data in Fig. 8a show that Γ(exp)(DF) > Γ(exp)($GdO_{1.5}$) > Γ(exp)($GdPd_3$), hence, f(DF) > f ($GdO_{1.5}$) > f($GdPd_3$). While, in the ε_0 data in Fig. 8b, ε_0($GdO_{1.5}$) > ε_0(DF) > ε_0($GdPd_3$), hence, f($GdO_{1.5}$) > f(DF) > f($GdPd_3$). That is, non-consistent result is obtained either here between the first two systems, depending on either Γ(exp) or ε_0 data are used. Though not detailed here, either for the lowest-y DF-type subphase ($\sim 0.18 \le y \le \sim 0.30$), such inconsistency results between the three systems. Since Γ(exp) and ε_0 data for the C-type $GdO_{1.5}$ and $GdPd_3$ are regarded as "distortion-free" intrinsic one, we should conclude that for all the SZ-type nonstoichiometric solid solutions ($\sim 0.18 \le y \le \sim 0.62$), due to the inherent "disorder (randomness)" of the system, significant spectrum distortion is indeed occurring in Figs. 8a,b. Naturally, we cannot apply eqs.

13a,b and 14 for such "distorted" non-intrinsic Γ(exp) and ε_0 data of these solid solutions on the same basis together with those of the former in Figs. 8a,b.

Fortunately, such spectrum distortion, i.e., the extra line-width broadening in the Γ(exp) and the accompanying peak-height reduction in the ε_0, tends to cancel out (compensate) with each other in their product, RAA [= Γ(exp)·ε_0] shown in Fig. 8c. In other words, the value of RAA, which represents the total amount of γ-ray quanta absorbed by the system, is essentially independent of such details of whether its components [Γ(exp) and ε_0] make either sharp or broad singlet, one unresolved-broad doublet or two well-resolved doublets, etc., i.e., whatever the individual compensating distortions they make. Indeed, the RAA data of these solid solutions shown in Fig. 8c exhibit "Γ(exp) and ε_0 well-mixed" regular behavior for which apparent irregularities of ε_0 data in Fig. 8b are removed. Combining the above eqs. 13a,b and 14

$$\text{RAA(norm)} = \text{RAA}/(f_S \cdot 2\Gamma) = (\Gamma(\text{exp})/2\Gamma)\cdot(\varepsilon_0/f_S) = \text{eq. 13a,b}\cdot\text{eq. 14} \quad (15)$$

The normalized RAA [= RAA(norm)] curves in eq. 15 are calculated by combining eq. 14 either with eq. 13a for the lower $0 < f < \sim 0.23$ range or with eq. 13b for the higher $\sim 0.19 < f < \sim 0.60$ range, and are drawn in Fig. 9 as solid lines. These two curves connect well with each other in the overlapping $\sim 0.19 < f < \sim 0.23$ range and exhibit a mixed [Γ(exp)·ε_0] monotonous increase with the f of the system. Thus, we can now in principle determine the f of the system (the abscissa value) using eq. 15, i.e., in Fig. 9, if we can fix the value of RAA(norm) [= RAA/(f_S·2Γ)] data (the ordinate value) for various-y solid solutions. That is, we need to know reasonably accurate values both of its numerator (the raw RAA data in Fig. 8c) and denominator (the normalization factor; f_S·2Γ).

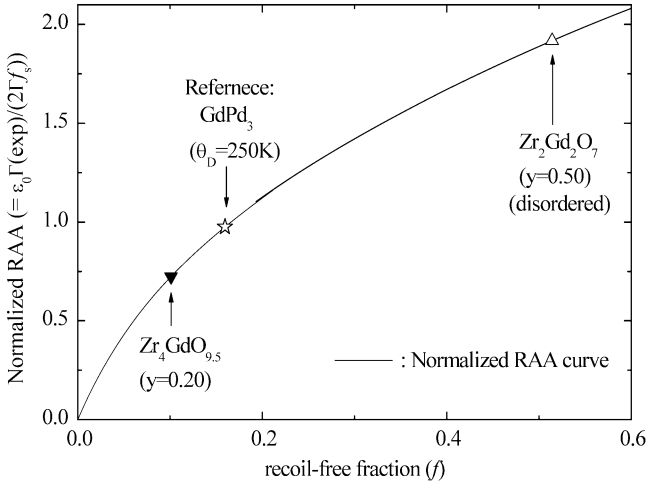

Fig. 9 Normalized RAA vs. f plot for ZrO_2–$GdO_{1.5}$ systems, $Zr_{1-y}Gd_yO_{2-y/2}$. Calculated curves according to eq. 15 are drawn as solid lines.

We could make not so bad an estimate for the normalization factor (f_S·2Γ) from the Γ(exp) and ε_0 data of $GdPd_3$ shown in Figs. 8a,b, isomorphic with the present γ-ray source, $^{155}Eu/^{154}SmPd$. (As a matter of fact, we have measured the ^{155}Gd spectrum of $GdPd_3$ using the latter [71], to evaluate the quality of the latter as a γ-ray source.) However, we should also encounter here with another problems associated with the raw RAA data themselves (in its numerator) shown in Fig. 8c; e.g., the true ^{155}Gd Mössbauer-spectrum, i.e., the true RAA is not of triangular in shape [Γ(exp)·ε_0, as expressed here for convenience] but of Lorenzian (or Gaussian) in shape, necessitating a correction factor (π/2 in the former). Moreover, besides the above-discussed spectrum distortion, not only the true Γ(exp) may need

correction for the instrumental line-broadening to the raw Γ(exp) data in Fig. 8a, but also the true ε_0 data need correction for the background γ-ray absorption to the raw ε_0 data in Fig. 8b, and so on. For many of these, the exact corrections are often not easy either in the present ^{155}Gd- or in any other Mössbauer experiment. This argument suggests the difficulty in dealing with the absolute value of RAA(norm) = RAA/(f_S·2Γ) in eq. 15, without which we cannot fix the ordinate value in Fig. 9, so we cannot determine the f (its abscissa value) of the system.

In order to bypass or avoid these difficulties in this direct method, the most commonly used method is to measure the Mössbauer spectra of a given sample over a wide temperature range (e.g., this is possible for ^{57}Fe compounds over the widest range from the lowest several Kelvin to the highest ~1200 K range) keeping the temperature of the Mössbauer γ-ray source (^{57}Co) constant (i.e., fixing its f_S·2Γ at some constant value). In short, from the temperature dependence of the obtained RAA data, Θ_D and f of the system are calculated using, e.g., the next equation; in the high-temperature approximation (instead of the low-temperature one, eq. 12): $\Theta_D^2 \cdot M \cdot \{-d[\ln(RAA)]/dT\} = 6E_R/k$ (i.e., RAA ∝ $f = \exp(-6\, E_R T/k\Theta_D^2)$ in the thin absorption-thickness (T_A) limit.) By utilizing the logarithm form of RAA data and taking their temperature (T) derivative, the problem associated with the normalization and correction factors (f_S·2Γand other correction constants) in RAA(norm) in eq. 15 is eliminated. In its most sophisticated version, the temperature dependence of RAA data of a given ^{57}Fe sample is measured in parallel with that of the reference material, e.g., Fe–Al alloy for which the f is well-known as a function of temperature. This method, though widely used, is only applicable for those measurable over wide temperature range with relatively low-energy γ-ray sources such as ^{57}Fe (~14 KeV), ^{151}Eu (~21.5 KeV), and ^{119}Sn (~23.9 KeV), etc. Unfortunately, this is hardly applicable for the present ^{155}Gd-Mössbauer case with high-energy γ-ray (86.5 KeV) only measurable up to ~several tens K.

Because of these several reasons, what we employ here is somewhat a technical method. In short, instead of dealing directly with the absolute values of these RAA data, those of the cubic $GdPd_3$ with a single kind of isotropic Gd–O bond are used as a reference. (Of course, the present and the "direct" methods should give the same, or at least consistent, results. The more complete description of the present treatment will be given as a separate paper including this consistency problem with the direct method.) For all the present systems shown in these figures, experimental Θ_D data are quite sparse, and reliable Θ_D estimation seems to be only possible for $GdPd_3$; in [74], from the low-temperature specific-heat data, Θ_Ds of several isomorphic $LnPd_3$ systems (Ln = La, Ce, Lu, Y, Sc) are reported to be 177, 299, 285, 312 and 337 K, respectively. Though all these Θ_Ds appear to converge around 300 K except for $LaPd_3$, the choice of Θ_D = 300 K for $GdPd_3$ (the melting point, T_m = 1630 °C = 1903 K) appears to be a little too high; this results in a very high Θ_D over 1200 K (Θ_D > 1200 K) for the ideal $Zr_2Gd_2O_7$ having the top high RAA in Fig. 8c and hence the highest Θ_D of all the present systems.

Thus, as a most reasonable choice at this stage, we have set Θ_D = 250 K for this $GdPd_3$ reference system as the arithmetic average of the reported Θ_Ds for the three true lanthanide systems (Ln = Ln, Ce, and Lu) (~254 K). In eq. 12, this choice of $\Theta_D(GdPd_3)$ = 250 K gives the value of its recoil-free fraction, $f(GdPd_3)$ = 0.1595 at 12 K. Then, in Fig. 9 (eq. 15), the value of RAA(norm) for $GdPd_3$ is determined to be 0.975. Since the ratio of RAA data between $GdPd_3$ and various-y DF solid solutions, RAA(DF)/RAA($GdPd_3$), is readily known in Fig. 8c, once this is fixed for $GdPd_3$, that of any-y DF system can be readily calculated. Then, we can determine its f in Fig. 9 and further its Θ_D in eq. 12. We show there the two extreme examples; $Zr_{0.8}Gd_{0.2}O_{1.9}$ [= (1/5)·$Zr_4GdO_{9.5}$] around the lower monoclinic/DF phase boundary (y = 0.20) and the disordered $Zr_2Gd_2O_7$ (y = 0.50) having the smallest and largest RAA in Fig. 8c and therefore the lowest and highest f and Θ_D, respectively.

The f and Θ_D data of all the present systems thus obtained are shown in Figs. 10a,b, respectively. By virtue of the interrelationships, eqs. 11–15, their original RAA data in Fig. 8c, and the derived f and Θ_D parameters in Figs. 10a,b, they all exhibit largely analogous characteristic behavior first clarified in the present detailed ^{155}Gd-Mössbauer study. Several salient features of these f and Θ_D data and what we can extract from these data as to the local structure and physicochemical properties of this Gd-SZ

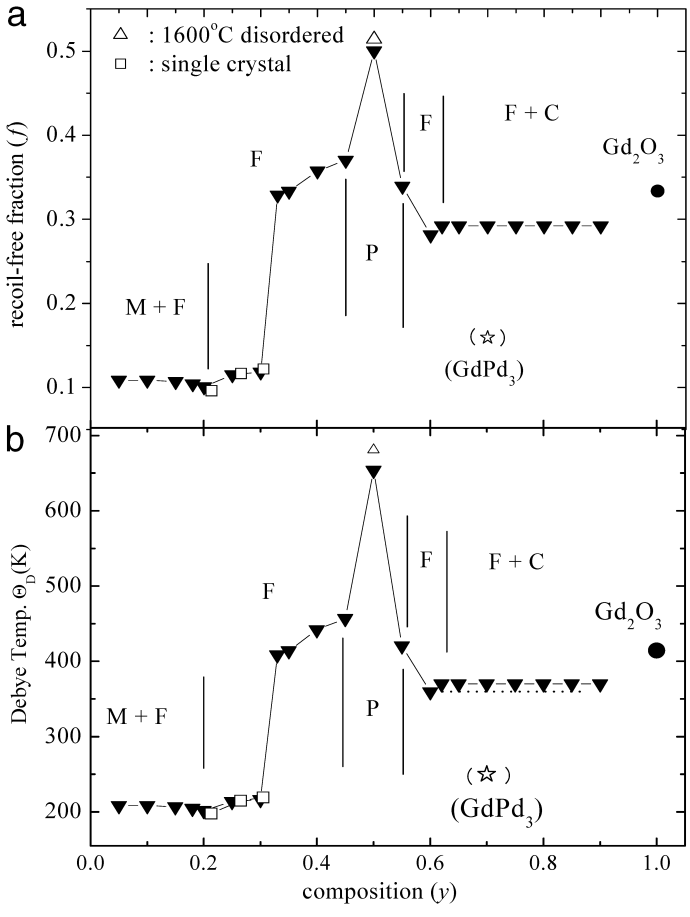

Fig. 10 (a) f vs. y plot for ZrO_2–$GdO_{1.5}$ systems, $Zr_{1-y}Gd_yO_{2-y/2}$. Line is a guide to the eye. (b) Θ_D vs. y plots for ZrO_2–$GdO_{1.5}$ systems, $Zr_{1-y}Gd_yO_{2-y/2}$. Line is a guide for the eye.

are discussed below in connection with available Θ_D and related basic property data of these SZs and DF oxides. In doing so, we note that the Θ_D of the system obtained in the Mössbauer method represents by its own nature the rigidity (stiffness) of local-lattice system in the vicinity of the Mössbauer nucleus (here ^{155}Gd) rather than that of the bulk crystal-lattice system as a whole. While, in the usual thermodynamic methods such as specific-heat, enthalpy, and sound-velocity measurements, the latter bulk Θ_D is obtained. The XRD and ND methods usually measuring the Debye–Waller factor of the system are considered to situate in between these two. We admit that the absolute values of here-obtained f and Θ_D inevitably contain some ambiguity dependent on the initial choice of $\Theta_D(GdPd_3)$. So, emphasis here is put on their composition (y) variations that are of more central concern in our present study.

1. The sharp maximum of both f and Θ_D at the ideal (stoichiometric) pyrochlore $Zr_2Gd_2O_7$ at $y = 0.50$ is quite evident, either XRD-ordered or -disordered (the either is judged to be the same within experimental error). This unequivocally evidences that the strongest near-ideal anisotropic P-type Gd–O bonding structure (CN = 8) (Fig. 1c) is formed here, reaching its $f \sim 0.50$ and $\Theta_D \sim 650$–675 K. First, compare this value of Θ_D with those of the two end members: For pure monoclinic ZrO_2 ($y = 0$), the reported bulk-thermodynamic Θ_Ds are 575 and 590 ± 20 K [75a], 747K [75b], and in [75c] even the temperature- and model-dependent Θ_D = 530–740 K is reported by Tojo et al. Though we are not aware of Θ_D data for the C-type $GdO_{1.5}$ ($y = 1.0$), those

of several other Ln_2O_3 (= 2·$LnO_{1.5}$) are available; Θ_D = 178 and 460 K for Y_2O_3 [76a,b], 280 K for Yb_2O_3 and 300 K for Lu_2O_3 [76c]. Though relatively large scatter exists for these reported Θ_D data, we judge that the $Zr_2Gd_2O_7$ has slightly or significantly larger Θ_D ~ 650–675 K than pure ZrO_2 (y = 0) or the C-type $GdO_{1.5}$ (y = 1.0), respectively. Also note that here-obtained Θ_D = 415 K for the latter is close to the reported highest 460 K for Y_2O_3 [76b].

In light of the above-mentioned nature of the Mössbauer f and Θ_D, these top-high values of f and Θ_D at y = 0.50 should undoubtedly represent the strongest characteristic axial-anisotropic Gd^{3+} bonding with the two short apical O2 (O2–Gd^{3+}–O2 bond; CN = 2) in Fig. 1c that can keep the ^{155}Gd nucleus recoil-free, rather than its supposedly much weaker Gd^{3+}–O1 bonds (CN = 6). The sharpness of these peaks at y = 0.50 in turn suggests that within the narrow DP homogeneity range (~0.45 ≤ y ≤ ~0.55) only by introducing slight cation off-stoichiometry (of the order Δy ~ ±0.05), the system loses significant portion of its P-type Gd–O2 bond strength, resulting in the marked reduction in f (~0.50 → ~0.35) and Θ_D (~650–675 K → ~450–430 K) (nearly to the comparable level with those of the C-type $GdO_{1.5}$). That is, the integrity of this characteristic axial-anisotropic Gd–O2 bond is rapidly degraded by cation substitutional disorder ($Gd^{3+}{}_A$ + $Zr^{4+}{}_B$ ↔ $Gd^{3+}{}_B$ + $Zr^{4+}{}_A$) and the accompanying oxygen and V_O disorder (e.g., $O1_{42f}$ + V_{O8b} ↔ O_{8b} + V_{O42f}) [8,9]. The fact that such reduction in f and Θ_D is definitely more pronounced in the Gd-rich region (0.5 < y ≤ ~0.62) than in the Gd-deficit region (~0.33 ≤ y < 0.50) is reasonable; in Fig. 1c, in the former, not only the A-site Gd^{3+} begins to have oxygen vacancies (V_Os) in the O2 site, thereby losing both the number and integrity of this characteristic strong O2–Gd^{3+}–O2 bonding structure, but also the excess Gd^{3+} starts occupying the B-site (CN = 6), making the weaker Gd^{3+}–O1 bond. While, in the latter, basically only the number of this Gd^{3+}–O2 bonds decreases.

2. There are several experimental Θ_D data for pyrochlore oxides derived from the specific-heat measurements; Θ_D = 351 K for the present $Zr_2Gd_2O_7$, 489 K for $Zr_2Nd_2O_7$, and 353 K for $Dy_2Ti_2O_7$ [77a–c], all typical for pyrochlore oxides [8]. (We are aware of no Θ_D data for off-stoichiometric DP systems (y ≠ 0.50).) The fact that these reported bulk Θ_Ds are considerably lower than the present Mössbauer Θ_D ~ 650–675 K seems natural, for, as mentioned above, the former represents the main contribution from the Gd–O1, and Zr–O1 bonds much larger in number but presumably much weaker than the minor Gd–O2 bond. While, in the first-principle calculations [77d], much higher Θ_D = 1080–980 K for $La_2(Hf, Zr)_2O_7$ and even higher 1200–1050 K for $Y_2(Hf, Zr)_2O_7$ are reported (the respective former and latter values for the M^{4+} = Hf and Zr, respectively). It is also possible to obtain such higher $\Theta_D(Zr_2Gd_2O_7)$ ~ 900–1000 K by choosing higher $\Theta_D(GdPd_3)$ ~ 275 K in the present treatment, though, as mentioned above, $\Theta_D(GdPd_3)$ ~ 300 K is somewhat too high resulting in $\Theta_D(Zr_2Gd_2O_7)$ > 1200 K.

Recently, Han et al. [77e] reported elaborate coupled ND and XAFS study on a titanate pyrochlore $Tb_2Ti_2O_7$. They have not only determined the individual Θ_Ds of all the constituent elements at each site [= 220 K (Tb), 610 K (Ti), 760 K (O1), and 980 K (O2)] but also derived the correlated Θ_Ds for the specific (A,B)–O bond; Θ_D(correlated) = 875 K (Tb–O2), 450 K (Tb–O1), and 600 K (Ti–O1). The highest Θ_D(correlated) = 875 K for the Tb–O2 bond means that there is correlated (concerted) vibration between Tb^{3+} and two apical O2, i.e., the strongest direct chemical bond exists between them in the P structure (Fig. 1c). It is judged that this Θ_D(correlated) for Tb–O2 bond in $Tb_2Ti_2O_7$ closely corresponds to the ^{155}Gd-Mössbauer Θ_D ~ 650–675 K in the present $Zr_2Gd_2O_7$. While, the thermodynamic bulk Θ_D of $Tb_2Ti_2O_7$ is supposed to correspond either to the composition average of the individual constituent-Θ_Ds (= 643 K) or to the average bond-Θ_D (= 575 K).

3. As to the lower-y side outer DF-type solid solution region (~0.18 ≤ y < ~0.45), this is to be divided into the two subphase fields separated by the discontinuous f and Θ_D jump at around y ~ 0.30–0.33. Its higher-y side subphase region for ~0.33 ≤ y < ~0.45 neighboring with the central long-range ordered P phase (~0.45 ≤ y ≤ ~0.55) is definitely considered to be the short-range

ordered DP-type phase; where f and Θ_D maintain their hill-like high values comparable with those of the C-type $GdO_{1.5}$, exhibiting only moderate composition (y) variation. Such behavior is reasonable, as discussed in the above Eu-Mössbauer study: In contrast to the Gd-excess (and oxygen-deficit) region ($y > 0.50$), in this Gd-deficit (and oxygen-excess) region, the Gd^{3+} can occupy a single stable A-site (CN = 8 constant), $[(Gd,Zr)_2]_A[Zr_2]_BO_6\ O_{1+x}$ ($x > 0$), which is more in detail expressed using the present notation for composition (y) as

$$[Gd_{4y}Zr_{2-4y}]_A\ [Zr_2]_B\ [O_6]_{42f}\ [O]_{8a}\ [O_{1-2y}V_{O2y}]_{8b}\ (\text{for } y \le 0.5) \tag{16}$$

Thus, here, they can retain strong P-type axial-anisotropic O2–Gd^{3+}–O2 bond. Only its A-site occupancy steadily deceases from 9/10 at $y = 0.45$ (= 9/20) to 2/3 at $y \sim 0.33$ (= 1/3). This means that when ~1/10 (= 10 %) of the A-site Gd^{3+} is substituted by the excess Zr^{4+} at $y \sim 0.45$, the system loses its long-range P-type order, giving rise to a significant reduction in the Gd^{3+}-Mössbauer f and Θ_D, and further when this A-site $Gd^{3+} \rightarrow Zr^{4+}$ substitution slightly exceeds 1/3 (= 33 %) at $y = 0.33$, the system can no longer sustain even its short-range P-type order, abruptly further loosing its structural integrity and its Gd–O2 bonding strength, as evidenced by a collapsing drop of its f and Θ_D.

As seen in the irregular ε_0 behavior in this region (Fig. 8b), the relatively high degree of DP-type structural disorder exists here; these are, as suggested in eq. 16 for the detailed DP-type chemical formula, the multiple oxygen sublattice disorders involving the major 48f O1, the apical 8a O2, and additionally 8b excess-oxygen and V_O, and the excess-Zr^{4+} in the A-site and the cation further site-exchange between the A-site Gd^{3+} and the B-site Zr^{4+}, etc. That is, all these cation and anion disorders do no more allow the system to keep the long-range ordered coherent P-type structure throughout the bulk crystal lattice, disrupting it into the fractals of only short-range ordered DP-type microdomain structure. Due to such inherent microscopic heterogeneity, the Gd^{3+}s here are supposed to have varieties of DP-type anisotropic (noncubic) Gd–O bonds mainly with CN = 8 (but probably also with CN = 7 or even 6), giving "unresolved" very broad single-doublet Mössbauer spectrum, i.e., significant spectrum distortion [the simultaneous Γ(exp) broadening and ε_0 reduction] in Figs. 8a,b. However, the system here seem to be still struggling to maintain its DP-type short-range order as wide as and as long as possible. When we trace the system in increasing y direction ($y = 0.33 \rightarrow 0.45$), it is here collectively working to attain macroscopic long-range P-type order above $y = 0.45$, e.g., by eliminating misaligned P-type anti-phase boundaries between the microdomains [2,60]. This is also consistent with the above-discussed rapid growth of the overall P-type QS in this region (Fig. 7c) and also the sharp decrease of IS(Eu^{3+}) in the same region in the Eu-SZ(SH) (Fig. 4b).

4. Then, the next questions are:
   a. Why does this system abruptly loose its DP-type short-range order at around $y \sim 0.30$–0.33?
   b. What is the local structure of the lowest-y side subphase below $y = 0.30$ at which the system finally arrives after such collapsing structural degradation around the Gd^{3+}?

Our answers to these two closely interrelated questions are in brief as follows:

a. This composition $y = 0.33$ just corresponds to the point at which the Zr^{4+}s take the average seven-fold oxygen coordination, CN(Zr^{4+}) = 7 (the same as that in the original monoclinic structure in pure ZrO_2), while the Gd^{3+}s are keeping its constant oxygen eight-fold coordination, CN(Gd^{3+}) = 8 in the detailed DP-type chemical formula in eq. 16. This can be easily shown generally by the following simple algebra (without going to the detailed eq. 16), as used in [78]

$$(1 - y)\cdot CN(Zr^{4+}) + y\cdot CN(Gd^{3+}) = 8 - 2y \tag{17}$$

where the right-hand side is the average oxygen coordination number (CN = $8 - 2y$) of the cations (Zr^{4+} + Gd^{3+}) in the present $Zr_{1-y}Gd_yO_{2-y/2}$ solid solution. Setting CN(Zr^{4+}) = 7 and CN(Gd^{3+}) = 8 in eq. 17 leads to the solution; $y = 1/3$ (= 0.33). This result means that

at $y = 0.33$ the system can be at a special state in which CN(Gd^{3+}) = 8 and CN(Zr^{4+}) = 7 in either y side, and, when the system approaches to $y = 0.33$ from the lower-y side, to realize this special oxygen coordination state in the higher-y side, instead of any other (disordered or ordered) structure, the system can choose (and in fact has chosen) by itself the DP-type structure expressed by eq. 16 as the most favorable one. The counter situation in the lowest-y side subphase region (~0.18 ≤ y ≤ ~0.30) is described in our next answer to the above question (b):

b. When locally probed by ^{155}Gd-Mössbauer nucleus, as is clearly evidenced by its very low (in fact, the lowest) near-constant ^{155}Gd-Mössbauer f (~0.10–0.11) and Θ_D (~200–210 K) in Figs. 10a,b, this lowest-y subphase (~0.18 ≤ y ≤< ~0.30) looks more like a "disordered" glassy (or amorphous) material having each-isolated random and weak Gd^{3+}–O bonds dilute-dispersed in its host ZrO_2 matrix lattice still retaining its original monoclinic structure in microscopic scale (CN ~ 7). That is, this initial Gd-stabilized cubic-zirconia subphase is basically the major-constituent ZrO_2-based DF phase deeply colored with its original monoclinic-type largely distorted DF structure with CN(Zr^{4+}) ~ 7. This interpretation seems consistent with several of the EXAFS local structure study in Table 1 that V_O tends to be adjacent to the smaller Zr^{4+}, and the dopant (Ln^{3+}) is the 2nd NN to V_O, i.e., CN(Zr^{4+}) ~ 7 and CN(Gd^{3+}) ~ 8. The important point here is that such oxygen coordination state in this disordered ZrO_2-based lowest-y side subphase just matches at $y = 0.33$ with that of the DP-type short-range ordered higher-y side subphase, as shown in eqs. 16–17, enabling the system to readily switch over between them at $y = 0.33$. One direct and convincing evidence for such parent ZrO_2-based presence of CN(Zr^{4+}) ~ 7 and CN(Y^{3+}) ~ 8 state in this lower-y side subphase region is recently obtained by Kawada, et al. in their ^{89}Y MAS-NMR study of YSZ [78].

Also, the ^{155}Gd-Mössbauer QS in this subphase in Fig. 7c is relatively small, almost comparable with that smaller of the major 24d site in the C-type $GdO_{1.5}$. Though it is certain that this subphase has also growing (superficially P-like) anisotropy around the Gd^{3+} in Fig. 7c, this would be interpreted as the overall slightly distorted nature of such various isolated Gd^{3+} sites (CN ~ 8) embedded in the distorted DF-type oxygen environment of its ZrO_2 matrix lattice. It is inferred that this stems from the tendency of the major Zr^{4+} to maintain its original CN ~ 7 in the monoclinic ZrO_2, thereby forcing the minor Gd^{3+} to take the higher-than-average oxygen coordination (i.e., CN ~ 8 > 7) in the vicinity of monoclinic/DF phase boundary region (y ~ 0.18). With increasing y (i.e., increasing Gd^{3+} and V_O concentration), the system gradually becomes aware of which direction to go, but, until approaching quite close to this critical composition (y ~ 0.30–0.33), the Gd^{3+} seems to remain in the near-random disordered site composed of each-isolated weak and distorted Gd–O bonds (CN ~ 8). The IS(Eu^{3+}) data of the Eu-SZ(SH) in this region were analyzed in Fig. 4b based on the P-type structure model. More properly, those should be reanalyzed from this ZrO_2-based structure model. However, if we regard the latter as a "disordered P-like" state in which almost the same coordination state [CN(Zr^{4+}) ~ 7 and CN(Gd^{3+}) ~ 8] is maintained only lacking its short-range order, no major revision would be necessary for there-obtained results.

Summarizing the above discussion, the present ^{155}Gd-Mössbauer evidences (the discontinuous jump of f and Θ_D plus related many findings) reveal that this phase transition occurring in a narrow composition range in-between $y = 0.30$ and 0.33 in this Gd-SZ system is a drastic local structure switchover (transformation) process from the largely distorted parent ZrO_2-based "disordered" monoclinic DF-type in the lower-y side to the more regularly ordered short-range DP-type one (eq. 16) in the higher-y side: Where, keeping nearly the same CN(Zr^{4+}) ~ 7 and CN(Gd^{3+}) ~ 8 state on either side (eqs. 16,17), the system can in a splendid manner improve its local-structural integrity around its minor

Gd^{3+} cations from the near-random "disordered" weak Gd–O bonds (CN ~ 8) to the uniquely axial-anisotropic strong Gd–O bonds (CN = 8) (Fig. 1c) in the (D)P-type structure.

Below, we make some final discussions of the present results in reference to the reported additional basic property data on these SZs and DF oxides.

As mentioned above, the reported Θ_D data of pure ZrO_2 ($y = 0$) ranges 530–740 K [75a–c], much higher than here-obtained ^{155}Gd-Mössbauer Θ_D ~ 200–210 K for the neighboring lowest-y side Gd-SZ (~0.18 ≤ y ≤ ~0.30). It is certain that the latter does not properly reflect Θ_D of the bulk crystal-lattice around the major Zr^{4+} but does represent that of the local-lattice around the minor Gd^{3+}. Yet, so far as the latter has much lower Θ_D than pure ZrO_2, if we measure the bulk Θ_D of the system in this subphase region, the measured Θ_D is expected to be lower to some extent than that of pure ZrO_2, for, as discussed above, this subphase is a "disordered" ZrO_2 phase and the main source of this "disorder" here is the minor $GdO_{1.5}$ F-stabilizer itself.

The Θ_D data reported for SZs and doped cerias in this lowest-y subphase region (~0.18 ≤ y ≤ ~0.30) are in line with this conjecture: Tojo et al. [75c] observed the lowering of Θ_D of pure ZrO_2 from the above-cited temperature and model-dependent Θ_D = 530–770 to 440–720 K for several YSZs (4, 8, 10, 11 mol % Y_2O_3); after the initial drop of about $\Delta\Theta_D$ ~ –50~90 K by 4 mol % Y_2O_3 doping, for all the 4–11 mol % Y_2O_3 systems (corresponding to y = 0.077–0.20), no subsequent Θ_D change was observed. In [79], for Ln-doped cerias (Ln = La, Sm, Dy, Y), the Θ_D from the sonic-wave velocity measurements is reported to steadily decrease from 480 K for pure ceria (CeO_2) ($y = 0$) to 466–441 K at $y = 0.1$ and further to 450–454 K at $y = 0.20$, almost independently of the kind of these Ln dopants. In both of these studies, it is proposed that the lattice softening caused by the introduction of disorder by aliovalent-Ln^{3+} and V_O doping is responsible for the observed lowering of Θ_D in these DF oxides. The degree of these bulk-Θ_D drop in either case is indeed modestly well within 100 degrees ($|\Delta\Theta_D| <$ 100 K). In this sense, we can say that the present ^{155}Gd-Mössbauer-Θ_D data demonstrate in a largely exaggerated fashion such initial lowering of Θ_D of the system by disorder effect in the lowest-y side subphase, by locally probing the system in the vicinity of the minor ^{155}Gd-Mössbauer nucleus. For the higher-y solid solution field up to $y = 0.62$, since the Gd content of the system is no more minor, this would become to reflect increasingly more the bulk Θ_D of the system. Unfortunately, to our knowledge, there seem to exist no literature (either bulk or local) Θ_D data for any SZ and related DF oxide that support or oppose the presently found two-step jump up of Θ_D to the maximum at the ideal pyrochlore $Zr_2Gd_2O_7$ at $y = 0.50$ in this Gd-SZ.

In comparison with the well-resolved two-doublets ^{155}Gd-Mössbauer spectrum obtained for the long-range V_O-ordered but defective C-type $GdO_{1.5}$ (Fig. 1b), very broad seemingly "unresolved" single-doublet spectra observed for almost all of these DF solid solutions in this Gd-SZ suggests that these all are most likely a microscopic composite mixture of varieties of intermediate P-based distorted noncubic Gd^{3+} (more generally Ln^{3+}) sites with CN = 8 (plus 7 and 6) having wide QS distribution, in a sense analogous to glassy (or amorphous) materials. It is rather surprising that even the ideal $Zr_2Gd_2O_7$ at $y = 0.50$ with crystallographic well-defined ideal pyrochlore structure (Fig. 1c) as a long-range ordered stoichiometric (1:1) intermediate compound between the pseudo F-type ZrO_2 and the C-type $GdO_{1.5}$ seems not free from such spectrum distortion: Even this system, which has consistently all the highest Γ(exp), ε_0, and RAA data in Figs. 8a–c, exhibit some spectrum distortion, as evidenced by apparently different shapes of these three Mössbauer parameters [Γ(exp), ε_0, RAA] in Figs. 8a–c around the maximum at y ~ 0.50, and thus seems to have some distribution of P-type noncubic Gd^{3+} sites not solely represented by the single characteristic axial-anisotropic Gd–O configuration (CN = 8) in Fig. 1c. This means that even this system would have significant amount of structural disorders such as the antisite cations and the accompanying oxygen sublattice disorder. Such structural disorder would be most enhanced in this system among all the SZs, present just in the vicinity of the macroscpic DF-P stability boundary region. This is generally believed to be the main origin for the onset of well-known peculiar second ionic-conductivity maximum at y ~ 0.50 in this system [5,9,21]. And this is plausibly also

the main origin for the reported high radiation tolerance of this Gd-SZ. Generally, the line compounds with high melting points (so high Θ_Ds) are not necessarily radiation tolerant due to their poor flexibility to adopt structural disorder. Accordingly, the high radiation tolerance of this Gd-zirconate pyrochlore $Gd_2Zr_2O_7$ is considered to stem from such fortunate combination of widely nonstoichiometric intermediate P-based long- and short-range ordered structure (phase) spreading over ~0.33 ≤ y ≤ ~0.62 region with there-involved strong chemical bond (high Θ_D). That is, this system is simultaneously enough tough and flexible to accommodate radiation-induced varieties of displacive and substitutional disorders and defects.

Many characteristic phase, structural, and physicochemical property changes of these SZs occurring at y ~ 0.30–0.33 are once again summarized here; these are, the broad a_0 hump over the extended stabilized DF phase region (~0.30 ≤ y ≤ ~0.60–0.80) for many SZ(SH)s, the appearance of P-type antiphase boundary in the XRD and ED data at y ~ 0.30 reported for this and several other SZs [2,60], the steeper IS(Eu^{3+}) change for y ≥ ~0.30 in Eu-SZ(SH) in Fig. 4b, and specifically on this system, the reported turning point (y ~ 0.30) of ionic conductivity from decreasing to increasing direction toward the second maximum at y = 0.50 [21], a subtle slope change of the ^{155}Gd-Mössbauer QS at y ~ 0.30 in Fig. 7c, and the drastic jump of ^{155}Gd-Mössbauer Γ(exp), ε_0, and RAA data in between y ~ 0.30 and ~0.33 in Figs. 8a–c, evidencing the sudden gain in f and Θ_D of the system (Figs. 10a,b), etc.

From the last ^{155}Gd-Mössbauer findings on the Gd-SZ, we have proposed a new local structure model for the lowest-y side DF subphase (~0.18 ≤ y ≤ ~0.30) as the parent ZrO_2-based largely distorted DF-type disordered phase. On this basis, we have further proposed a possible mechanism of this phase transition at y = 0.33 from the disordered DF-type to the short-range ordered P-type, giving a simple explanation why this takes place at y = 0.33 (eqs. 16–17). According to the original proposal of Burggraaf et al. [21–25], this unique stabilized DF phase in SZ(SH)s was denoted as the F–P hybrid phase, and further divided into the two subphase regions; the main F-type matrix phase embedding in it the minor P-type microdomain for the lower ~0.18 ≤ y ≤ ~0.30 region, and inversely the main P-type matrix phase embedding in it the minor F-type microdomain for the higher ~0.30 < y ≤ ~0.45 region. While, in our present proposal, in the former, "the P-type microdomain" embedded in "the DF-type matrix phase" had better be more deliberately rewritten to "the dopant (Gd^{3+})-containing disordered DF region" embedded in "the parent ZrO_2-based distorted DF-type matrix phase". If this transition is the main- and sub-players' role-exchange process (i.e., main DF + sub P in the lower-y side → main P + sub DF in the higher-y side) in which the relative fraction of DF- and P-phases is changing smoothly, it seems difficult to rationalize the occurrence of so many definite and sometimes even discontinuous, phase, structural, and physicochemical property changes at y = 0.33 in many SZs. Also in this sense, the present proposal that defines this transition as a local structure transformation between "the crystallographic essentially different" distorted ZrO_2-based DF-type disordered phase and the short-range ordered DP-type phase seems more reasonable.

Furthermore, while Burggraaf et al. [21] once called this structural change between these two subphases at y ~ 0.30–0.33 "diffuse" phase transition, as evidenced in the present ^{155}Gd-Mössbauer data in Figs. 8a–c and 10a,b, this seems to be a sharp-enough phase transition in which the system acquires a huge gain in f and Θ_D within such a narrow composition interval; y ~ 0.30–0.33. One may regard this as a collective and synergetic disordered DF → ordered P local structure transformation, strengthening drastically its anisotropic Gd–O bond.

Thus, through the present comprehensive studies, we have clarified that the so-called SZs and their Hf analogs (SHs) have essentially different local structure and phase over the entire cubic DF-type solid solution region (~0.15–0.18 ≤ y ≤ ~0.70–0.80) from the parent F-based M^{4+} = Ce, U, and Th systems. In the latter larger M^{4+} systems, basically a naïve DF-type solid solutions with near-random (or only short-range ordered) cation (M^{4+}, Ln^{3+}) and anion (O^{2-}, V_O) distribution in each sublattice are formed between the two end members, i.e., the parent F-type MO_2 (Fig. 1a) and the C-type $LnO_{1.5}$ (Fig. 1b). In contrast, in these SZ and SH systems with much smaller M^{4+} (= Zr, Hf) than either Ln^{3+}

or the above M^{4+}, initially the Ln^{3+}-stabilized largely distorted parent ZrO_2-based DF-type phase in which CN(Zr^{4+}) ~ 7 and CN(Ln^{3+}) ~ 8 is formed for the lowest-y side (~0.15–0.18 ≤ y ≤ ~0.30), then, this transforms to the short-range ordered DP-type phase at around y ~ 0.33, keeping nearly the same oxygen coordination state for the both constituent cations but improving tremendously its structural integrity, and at y ~ 0.45, this further transforms to its long-range ordered P-type phase extended over ~0.45 ≤ y ≤ ~0.55, finally realizing its ideal P structure $Zr_2Ln_2O_7$ (Fig. 1c) at y = 0.50.

CONCLUDING REMARKS

In this paper, we have given a rather lengthy up-to-date summary of our coupled macroscopic (a_0) and microscopic Ln(= ^{155}Eu and ^{151}Gd)-Mössbauer studies of grossly oxygen-deficit highly defective DF oxides $M_{1-y}Ln_2O_{7-y/2}$ (M^{4+} = Hf, Zr, Ce, U, Th; Ln^{3+} = trivalent lanthanide) of significant technological importance. Through these studies, the intermediate P-based local structure of the so-called SZs and its Hf analog, SHs (M^{4+} = Zr and Hf), seem to have been almost unambiguously clarified with different (from the conventional) approaches: These are:

1. The presence of a broad a_0 hump over the extended stabilized cubic-DF region (y = ~0.3 – ~0.7) that has been first revealed from our detailed a_0 analysis according to the proposed a_0 model applicable for all these DF oxides.
2. The microscopic ^{151}Eu-Mössbauer evidence of Eu^{3+} ISs showing characteristic V-shaped minima around the ideal-P area (y ~ 0.50) for both the Eu-SZ and Eu-SH, distinctively different from those of the parent F-based M^{4+} = Ce, U, and Th systems. These data give a clear-cut almost direct evidence for the P-based local structure nature of SZs and SHs.
3. Rich ^{155}Gd-Mössbauer data on the $Zr_{1-y}Gd_yO_{2-y/2}$ [IS, QS, Γ(exp), ε_0 and RAA] revealing the formation of long-range ordered P phase for ~0.45 ≤ y ≤ ~0.55 with its highest Θ_D at y = 0.50 and its deep penetration into the outer "disordered" stabilized DF-type region as a short-range ordered P-type phase on either side. These data provide us with valuable information on the detailed DF-P phase and structure relationships in SZs. High radiation tolerance of the present pyrochlore $Gd_2Zr_2O_7$ has also been discussed in this context.

What we have done in this paper, in a word, was to clarify how the oxygen vacancy (V_O) interacts with its birthparents, i.e., various combinations of M^{4+} and Ln^{3+} (which inevitably introduce a fixed amount of V_O in the anion sublattice), to form different local and crystal structure of the solid solutions: In the parent F-based larger M^{4+} = Ce and Th systems for which the a_0 mismatch between the end members are relatively small, this is more or less a naïve random mixture-type solid solution between the parent F-type MO_2 (at y = 0) (Fig. 1a) and its superstructure, the C-type $LnO_{1.5}$ (at y = 1.0) (Fig. 1b). In the M^{4+} = U system, due to one other freedom of the U^{4+} (easy oxidation to U^{5+}), V_O itself is annihilated. And in the smaller M^{4+} = Hf and Zr systems in which monoclinic pure ZrO_2 and HfO_2 need to be stabilized first into the cubic-DF structure by substitutions of these $LnO_{1.5}$s, V_O is found to rather strongly interact with their parents (M^{4+} and Ln^{3+}) to form an intermediate P-type much more involved either short- or long-range ordered structure (Fig. 1c), associating itself with the smaller M^{4+}. The major driving force for such extensive local as well as crystal structural ordering here seems to be the ionic-radii mismatch of the parent cations (the smaller M^{4+} = Zr, Hf) with the larger Ln^{3+}; ($r_C(Ln^{3+})/r_C(M^{4+})$ >> 1) that give rise to strong local distortion and lattice-mismatch and lead the smaller M^{4+} (the larger Ln^{3+}) to strong preferential association with (dissociation from) V_O, so as to relax and minimize such local distortion and strain effect. In other words, the larger Ln^{3+} and the smaller Zr^{4+} (Hf^{4+}) intend to have the higher and the lower numbers of 1st NN oxygens than the average CN = 8 – 2y, respectively, i.e., CN(Ln^{3+}) > CN(M^{4+}), to minimize the repulsion between the coordinating oxygens. In the ideal pyrochlore structure (Fig. 1c), these reach the limiting CN(Ln^{3+}) = 8 and CN(M^{4+}) = 6.

Such local distortion and lattice-mismatch effects have been discussed rather extensively in connection with phase, a_0, and P- and C-type superstructure formation from the parent F structure (the distortional expansion of the crystal lattice and of the coordination polyhedron, etc.). In addition, we have also clarified that these are reflected not only in the monoclinic distorted structure of pure ZrO_2 (and pure HfO_2) but also in the local structure of their initial SZ- (and SH)-type solid solutions (~0.18 ≤ y ≤ ~0.30) formed at around the lower monoclinic/DF phase boundary region; this phase is most plausibly judged to be a largely distorted ZrO_2-based disordered DF-type one microscopically still remaining much of its original monoclinic structure of pure ZrO_2 (and HfO_2) [CN(Zr^{4+}) ~ 7 and so CN(Gd^{3+}) ~ 8]. On this basis, we have further proposed a possible mechanism of phase transition at y ~ 0.30–0.33 as the largely distorted disordered DF-type → the more regularly ordered short-range P-type local-structural transformation of the system through which SZ(SH)s exhibit many macroscopically observable phase, structural, and physicochemical property changes.

However, we had almost no space to discuss one of the most important properties of these DF oxides, that is, ionic conductivity (σ) mediated via V_O, therefore expected to most sensitively reflect such defect(V_O)-related local as well as crystal structural distortion and lattice-mismatch effects. Since this problem of ionic-conduction mechanism in these DF oxides is a formidable subject of which much still remains for the future study, we only briefly and qualitatively mention this at the end of the present paper: First in Fig. 4a, covering the wide range of M^{4+} from the largest Th to the smallest Hf, the general trend of ionic conductivity of these DF systems is, Ce > Zr > Hf ≥ Th [5], suggesting that indeed the lattice and ionic-radii mismatches between MO_2(M^{4+}) and $LnO_{1.5}$(Ln^{3+}) crucially affect their ionic conductivity. Such behavior corresponds well to there-observed phase-diagram trend of these systems that becomes more complicated with increase in such mismatches. Secondly, in Figs. 2b,c, the lower monoclinic/cubic-DF phase boundary region around which the maximum conductivity of SZs is observed corresponds to the here-defined distorted ZrO_2-based disordered DF-type phase region (y ~ 0.15–0.18), and there the maximum conductivity becomes higher for the smaller and heavier Ln^{3+}s (= Y, Er, Dy, etc.). As is apparent in these figures, this is because these smaller Lns have smaller lattice-mismatch and local distortion effects with even smaller Zr^{4+}(ZrO_2) and Hf^{4+}(HfO_2), and they indeed have much wider solid solution ranges (and simple phase diagrams) than the P-forming larger Eu^{3+}($EuO_{1.5}$) (Fig. 4a), Gd^{3+}($GdO_{1.5}$) (Fig.7a), and others.

In their extreme, the highest conductivity among all the SZs is observed in the smallest light-Ln^{3+} = Sc-SZ: $ScO_{1.5}$ has the smallest lattice parameter even smaller than the pseudo-F-type ZrO_2 and HfO_2, as seen in Fig. 3a. Compared with those larger Ln^{3+} dopants, such smaller Ln^{3+} dopants (the non-P-forming smallest three Ln^{3+} = Lu, In, and Sc) would probably have the higher number of 1st NN V_Os than the former and possibly even than the host Zr^{4+} and Hf^{4+} in their disordered ZrO_2-based stabilized phases. This factor may explain such higher maximum conductivity of the smaller dopant systems. For Ln^{3+} = In and Sc systems which have smaller a_0(C)/2 than a_0(F) of pure ZrO_2 and HfO_2 [i.e., a_0(C)/2 < a_0(F)] in Fig. 3a, even inversed conductivity trend that σ(SH) > σ(SZ) may be found, for here the lattice mismatch between the end members is smaller for the smaller M^{4+} = Hf than the larger Zr, contrary to the majorities of these SZs and SHs having larger dopants than themselves [i.e., a_0(C)/2 > a_0(F)]. However, this Sc-SZ is reported to be largely meta or even unstable, the cubic-DF phase decomposing and the ionic conductivity degrading with time during high-temperature operation as solid electrolyte. In view of reported phase diagram showing very narrow cubic DF-type stabilized phase region (~0.15 < y < 0.25) [38], r_c(VI)(Sc^{3+}) = 0.0745 nm in Fig. 3a seems to be a little too small to fully stabilize the cubic-DF phase, suggesting the possible role of P-type ordering and distortional expansion of the system for this cubic-DF stabilizaton. Yet, irrespective of the presence of similar problem, magnesia (MgO)-SZ with even smaller divalent dopant Mg^{2+} [r(VI) = 0.072 nm] [32] is still commercially available solid oxide electrolyte.

We hope that this summary report will help promote our basic understanding of these technologically important highly defective oxides and give some suggestions and stimulus for future studies on these systems.

ACKNOWLEDGMENT

The author (A. Nakamura) appreciates Prof. Masashi Takahashi of Toho University for his valuable discussion in the ^{155}Gd Mössbauer part of the present paper.

REFERENCES

1. T. Uehara, K. Koto, S. Emura, F. Kanamaru. *Solid State Ionics* **23**, 331 (1987).
2. T. Moriga, S. Emura, A. Yoshiasa, S. Kikkawa, F. Kanamaru, K. Koto. *Solid State Ionics* **40/41**, 357 (1990).
3. D. Komyoji, A. Yoshiasa, T. Moriga, S. Emura, F. Kanamaru, K. Koto. *Solid State Ionics* **50**, 291 (1992).
4. O. T. Sørensen (Ed.). *Nonstoichiometric Oxides*, Academic Press, New York (1981).
5. A. S. Nowick. *Diffusion in Crystalline Solids*, G. E. Murch, A. S. Nowick (Eds.), pp. 143–188, Academic Press, New York (1984).
6. T. Fujino, C. Miyake. In *Handbook on the Physics and Chemistry of the Actinides*, Vol. 6, A. J. Freeman, C. Keller (Eds.), Chap. 3, pp. 155–240, Elsevier Science, Amsterdam (1991).
7. N. Sakai, K. Yamaji, T. Horita, Y. P. Xiong, H. Yokokawa. In *Handbook on the Physics and Chemistry of Rare Earths*, Vol. 35, K. A. Gschneidner Jr., J.-C. G. Bünzli, V. K. Pecharsky (Eds.), pp. 1–43, Elsevier, Amsterdam (2005).
8. M. A. Subramanian, G. Aravamudan, G. V. Subba Rao. *Prog. Solid State Chem.* **15**, 55 (1983).
9. L. Minervini, R. W. Grimes. *J. Am. Ceram. Soc*. **83**, 1873 (2000).
10. A. Nakamura, J. B. Wagner Jr. *J. Electrochem. Soc.* **127**, 2325 (1980).
11. A. Nakamura, J. B. Wagner Jr. *J. Electrochem. Soc.* **133**, 1542 (1986).
12. M. F. Lasker, R. A. Rapp. *Z. Phys. Chem. NF* **49**, 198 (1966).
13. R. N. Blumenthal, F. S. Brugner, G. E. Garnier. *J. Electrochem. Soc.* **120**, 2320 (1973).
14. C. Degueldre, U. Kasemeyer, F. Botta, G. Ledergeber. *Mater. Res. Soc. Symp. Proc*. **412**, 15 (1996).
15. K. E. Sickafus, Hj. Matzke, Th. Hartmann, K. Yasuda, J. A. Valdez, P. Chodak III, M. Nastasi, R. A. Verral. *J. Nucl. Mater*. **274**, 66 (1999).
16. S. X. Wang, B. D. Begg, L. M. Wang, R. C. Ewing, W. J. Weber, K. V. G. Kutty. *J. Mater. Res.* **14**, 4470 (1999).
17. W. J. Weber, R. C. Ewing. *Science* **289**, 2051 (2000).
18. R. C. Ewing, W. J. Weber, J. Lien. *J. Appl. Phys*. **95**, 5949 (2004).
19. C. O'Driscoll. *Chem. Br*. Jan., 16 (2001).
20. K. E. Sickafus, L. Minervini, R. W. Grimes, J. A. Valdez, M. Ishimura, F. Li, K. J. McClellan, T. Hartmann. *Science* **289**, 748 (2000).
21. T. Van Dijk, K. J. de Vries, A. J. Burggraaf. *Phys. Status Solidi A* **58**, 115 (1980).
22. A. J. Burggraaf, T. Van Dijk, M. J. Verkerk. *Solid State Ionics* **5**, 519 (1981).
23. M. P. Van Dijk, K. J. de Vries, A. J. Burggraaf. *Solid State Ionics* **9/10**, 913 (1981).
24. M. P. Van Dijk, A. N. Cormack, A. J. Burggraaf, C. A. Catlow. *Solid State Ionics* **17**, 159 (1981).
25. M. P. Van Dijk, F. C. Mulhoff, A. J. Burggraaf. *J. Solid State Chem*. **62**, 377 (1986).
26. D. Steele, B. E. Fender. *J. Phys. C: Solid State Phys.* **7**, 1 (1974).
27. M. Morinaga, J. B. Cohen. *Acta. Crystallogr., Sect. A* **36**, 520 (1980).
28. M. H. Tuller, J. D.-Ghys, H. Dexpert, P. Lagarde. *J. Solid State Chem*. **69**, 153 (1987).
29. M. Cole, C. R. A. Catlow, J. P. Dragun. *J. Phys. Chem. Solids* **51**, 507 (1990).
30. H. Otobe, A. Nakamura. *Solid Oxide Fuel Cells (SOFC)-VI*, Electrochem. Soc. Proc. **99-19**, p. 463, NJ (1999).

31. (a) N. M. Masaki, N. R. D. Guillermo, H. Otobe, A. Nakamura, Y. Izumiyama, Y. Hinatsu. In *Mass and Charge Transport in Inorganic Materials: Fundamentals to Devices, Part A*, P. Vincenzini, V. Buscaglia (Eds.), p. 1233, TECHNA, Faenza (2000); (b) D. Harada, Y. Hinatsu, N. M. Masaki, A. Nakamura. *J. Am. Ceram. Soc.* **85**, 647 (2002); (c) N. M. Masaki, H. Otobe, A. Nakamura. *Hyperfine Interact. C* 305 (2003); (d) N. M. Masaki, H. Otobe, A. Nakamura, D. Harada, K. Ito, Y. Sasaki, Y. Hinatsu. *J. Nucl. Sci. Technol.* Suppl. **3**, 217 (2002); (e) N. M. Masaki, H. Otobe, A. Nakamura, D. Harada, Y. Hinatsu. *Mater. Res. Bull.* **40**, 650 (2005); (f) N. M. Masaki, A. Nakamura, F. Furuuchi, Y. Hinatsu. *J. Phys. Chem. Solids* **66**, 312 (2005).
32. R. D. Shannon. *Acta Crystallogr., Sect. A* **32**, 751 (1976).
33. (a) J. Wang, A. Nakamura, M. Takeda. *Solid State Ionics* **164**, 185 (2003); (b) J. Wang, H. Otobe, A. Nakamura, M. Takeda. *J. Solid State Chem.* **176**, 105 (2003); (c) A. Nakamura, H. Otobe, J. Wang, M. Takeda. *J. Phys. Chem. Solids* **66**, 35 (2005); (d) J. Wang, M. Takeda, A. Nakamura. *J. Nucl. Mater.* **340**, 33 (2005).
34. I. C. Cosentino, R. Muccillo. *Mater. Lett.* **48**, 253 (2001).
35. D. J. Kim. *J. Am. Ceram. Soc.* **72**, 1415 (1989).
36. R. P. Ingel, D. Lewis III. *J. Am. Ceram. Soc.* **69**, 1415 (1986).
37. V. I. Aleksandrov, G. E. Valyano, B. V. Luken, V. V. Osiko, A. E. Cautbort, V. M. Tatarintsev, V. N. Filatova. *Izv. Akad. Nauk. SSSR, Neorg. Mater.* **12**, 273 (1976).
38. (a) M. Yashima, N. Ishizawa, M. Yoshimura. *J. Am. Ceram. Soc.* **75**, 1541 (1992); (b) M. Yashima, N. Ishizawa, M. Yoshimura. *J. Am. Ceram. Soc.* **75**, 1550 (1992).
39. A-an Zen. *Am. Mineral.* **41**, 523 (1956).
40. C. P. Kempter. *Phys. Status Solidi* **18**, K117 (1966).
41. P. P. Porta, A. Anichini. *J. Chem. Soc. Faraday Trans. 1* **76**, 2448 (1980).
42. V. Grover, A. K. Tyagi. *J. Nucl. Mater.* **305**, 83 (2002).
43. (a) F. A. Mumpton, R. Roy. *J. Am. Ceram. Soc.* **43**, 234 (1960); (b) H. Radzewitz. KFK433 (1966).
44. (a) Y. Hinatsu, T. Fujino. *J. Solid State Chem.* **60**, 244 (1985); (b) Y. Hinatsu, T. Fujino. *J. Solid State Chem.* **63**, 250 (1986).
45. P. Duwez, E. Loh. *J. Am. Ceram. Soc.* **40**, 321 (1957).
46. E. C. Subbarao, P. H. Sutter, J. Hrizo. *J. Am. Ceram. Soc.* **48**, 443 (1965).
47. T. Kudo, H. Obayashi. *J. Electrochem. Soc.* **122**, 142 (1975).
48. J. D. Mucllourgh. *J. Am. Chem. Soc.* **72**, 1386 (1950).
49. R. T. Dirstine, R. N. Blumenthal, T. F. Kuech. *J. Electrochem. Soc.* **126**, 264 (1979).
50. M. R. Thornber, D. J. M. Bevan, E. Summerville. *J. Solid State Chem.* **1**, 545 (1970).
51. P. Duran, C. Pascual, J. P. Coutures, S. R. Skaggs. *J. Am. Ceram. Soc.* **66**, 101 (1983).
52. F. M. Spiridinov, L. M. Komissarova. *Zh. Neorg. Khim.* **15**, 875 (1970).
53. A. I. Ioffe, D. S. Ruthman, S. V. Karpachov. *J. Phys. Chem. Solids* **23**, 141 (1977).
54. R. E. W. Casselton. *Phys. Status Solidi A* **2**, 571 (1070).
55. J. Leferire. *Ann. Chim.* **8**, 117 (1963).
56. W. Baukel, R. Sheidegger. *Ber. Dtsch. Keram. Soc.* **45**, 611 (1968).
57. V. S. Stubican, R. C. Hink, S. P. Roy. *J. Am. Ceram. Soc.* **61**, 17 (1978).
58. JCPDS Powder Diffraction File^{TM} (Inorganic Phases) (1941–2001) and its subsequent CD-ROM version, International Centre for Diffraction Data, PA, USA.
59. J. J. Katz, G. Seaborg, L. S. Morss. In *The Chemistry of the Actinide Elements*, Vol. 2, p. 1156, Chapman and Hall, New York (1986).
60. D. Michel, M. Perez, Y. Jorba, R. Collongues. *Mater. Res. Bull.* **9**, 1457 (1974).

61. (a) V. I. Goldanskii, E. F. Markov. In *Chemical Applications of Mössbauer Spectroscopy*, V. I. Goldanskii, R. H. Herber (Eds.), p. 103, Academic Press, New York (1968); (b) N. N. Greenwood, T. C. Gibb. *Mössbauer Spectroscopy*, Chapman and Hall, London (1971); (c) G. Czjzek. In *Mössbauer Spectroscopy Applied to Magnetism and Materials Science*, Vol. 1, G. J. Long, F. Grandjean (Eds.), Chap. 9, Plenum Press, New York (1993); (d) H. Sano. *Mössbauer Spectroscopy, The Chemical Application*, Kodansha, Tokyo (1972) (in Japanese).
62. P. D. Battle, T. C. Gibb, P. Lightfoot, D. C. Munro. *J. Solid State Chem*. **83**, 31 (1989).
63. C. L. Chien, A. W. Sleight. *Phys. Rev. B* **18**, 2031 (1978).
64. (a) H. Armon, E. R. Bauminger, A. Diamant, I. Nowik, S. Ofer. *Solid State Commun*. **15**, 543 (1973); (b) E. R. Bauminger, A. Diamant, I. Felner, I. Nowik, S. Ofer. *Phys. Lett. A* **50**, 321 (1974); (c) E. R. Bauminger, A. Diamant, I. Felner, I. Nowik, A. Mustachi, S. Ofer. *J. Phys. Colloque C6,* **T37**, C6–47 (1976); (d) B. D. Dunlop, G. K. Shenoy, J. M. Friedt, M. Meyer, G. J. McCarthy. *Phys. Rev*. *B* **18**, 1936 (1978).
65. S. Tanabe, K. Hirao, N. Soga. *J. Non-Cryst. Solids* **113**, 178 (1989).
66. C. Keller, U. Berndt, H. Engener, L. Leiter. *J. Solid State Chem*. **4**, 453 (1972).
67. A. Nakamura, K. Yoshii. *J. Nucl. Sci. Technol.* Suppl. **3**, 160 (2002).
68. (a) A. Nakamura. *Z. Phys. Chem*. **207**, 223 (1998); (b) C. Miyake, T. Isobe, S. Imoto. *J. Nucl. Mater.* **152**, 64 (1988).
69. (a) I. D. Brown. In *Structure and Bonding in Crystals*, Vol. II, M. O'Keeffe, A. Navrotsky (Eds.), Chap. 14, pp. 1–30, Academic Press, New York (1981); (b) I. D. Brown. *The Chemical Bond in Inorganic Chemistry*, IUCr Mongraphs on Crystallograpy-12, Oxford University Press, Oxford (2002).
70. S. M. Haile, S. Meilicke. *Mater. Res. Soc. Proc.* **398**, 599 (1995).
71. J. Wang, M. Takeda, T. Shishido. *J. Nucl. Mater.* **340**, 52 (2004).
72. M. Zinkevich, Ch. Wang, F. M. Morales, M. Rühle, F. Aldinger. *J. Alloys Compd.* **398**, 261 (2005).
73. W. A. Barton, J. D. Cashion. *J. Phys. C* **12**, 2897 (1979).
74. M. J. Besnus, J. P. Kappler, A. Meyer. *J. Phys. F: Metal Phys.* **13**, 597 (1983).
75. (a) C. Degueldre, P. Tissot, H. Lartigue, M. Pouchon. *Thermochim. Acta* **403**, 267 (2003); (b) M. V. Nevitt, Y. Fang, S.-K. Chan. *J. Am. Ceram. Soc.* **73**, 2502 (1990); (c) T. Tojo, T. Atake, T. Mori, H. Yamamura. *J. Chem. Thermodyn.* **31**, 831 (1999).
76. (a) H. W. Goldstein, E. F. Nelson, P. W. Walsh, D. White. *J. Phys. Chem*. **63**, 1445 (1959); (b) B. M. Walsh, J. M. McMahon, W. C. Edwards, N. P. Barnos, R. W. Equall, R. L. Hutcheson. *J. Opt. Soc. Am.* **19**, 2893 (2002); (c) H. Li, C. Y. Wu, J. C. Ho. *Phys. Rev*. *B* **49**, 1447 (1994).
77. (a) S. Lutique, P. Javorsky, R. M. J. Konings, J.-C. Krupa, A. C. G. van Genderen, J. C. van Miltenburg, F. Wastin. *J. Chem. Thermodyn.* **36**, 609 (2004); (b) S. Lutique, P. Javorsky, R. M. J. Konings, A. C. G. van Genderen, J. C. van Miltenburg, F. Wastin. *J. Chem. Thermodyn.* **35**, 955 (2003); (c) Z. Hiroi, K. Matsuhira, S. Takagi, T. Tayama, T. Sakakibara. *J. Phys. Soc. Jpn*. **72**, 411 (2003); (d) J. M. Pruneda, E. Artacho. *Phys. Rev. B* **72**, 085107 (2005); (e) S. W. Han, J. S. Gardner, C. H. Booth. *Phys. Rev. B* **69**, 024416 (2004).
78. K. Kawata, H. Maekawa, T. Nemoto, T. Yamamura. *Solid State Inonics* **177**, 1687 (2006).
79. T. Hisashige, Y. Yamamura, T. Tsuji. *J. Alloys Compd.* **408–412**, 1153 (2006).